Improvement of the Characterisation of Nonmetallic Inclusions Especially Focusing on High Purity Steels for Aeronautic Applications

Master Thesis

submitted by

Susanne Penz
Chair of Metallurgy
Montanuniversität Leoben

Leoben, June 2007

Master Thesis

S 648

The Chair of Metallurgy poses
the following master thesis topic
to **Susanne Penz**:

Improvement of the Characterisation of Nonmetallic Inclusions Especially Focusing on High Purity Steels for Aeronautic Applications

The demands on steels for aeronautic applications are constantly rising, whereby the cleanliness plays an decisive role. New methods for the characterisation of nonmetallic inclusions permit a more sophisticated access to answering questions of formation and modification of nonmetallic inclusions. The master thesis is conducted in cooperation with Böhler Edelstahl GmbH.

Contents:

- **General specification of the selected steel grade (PH 13-8 Mo).**
- **Description and evaluation of selected methods for inclusion characterisation.**
- **Modification of an existing inclusion cluster for special Böhler-steel grades (martensitic and precipitation hardenable steels).**
- **Improvement of existing and development of new inclusion classes for a better characterisation of nonmetallic inclusions.**
- **Comparison of the P-SEM and INCA methods.**
- **Software adaptation.**
- **Variation of influencing measurement parameters.**

Leoben, October 2006 Univ.Prof. DI Dr.mont. Wilfried Krieger

Weiterentwicklung der Einschlusscharakterisierung im Bezug auf höchstreine Stähle für die Luftfahrt

Masterarbeit
eingereicht von

Susanne Penz

Kurzfassung

Aufgrund der stetig steigenden Qualitätsanforderungen an höchstreine Stähle für die Luftfahrtindustrie, gewinnt eine zuverlässige Erfassung von nichtmetallischen Einschlüssen zunehmend an Bedeutung. In der vorliegenden Arbeit werden verschiedene Methoden der Einschlusscharakterisierung beschrieben, wobei der Fokus im Bereich automatisierter REM/EDX Analysen liegt. Auf Basis erster Untersuchungen wird ein aus 25 Einschlussklassen bestehendes, speziell auf den Stahl PH 13-8 Mo abgestimmtes, Klassifikationssystem entwickelt, welches eine Einschlusstypisierung über den gesamten Herstellungsprozess ermöglicht. Neben dem Vergleich mit einer ähnlichen Analysenmethode (P-SEM) und der Variation verschiedener Einflussparameter, wird ebenso die Repräsentativität dieser Methode geprüft bzw. die Anwendbarkeit des Einschlusskataloges auf andere ausgewählte Stahltypen untersucht. Die Ergebnisse unterstreichen das Potential dieser Analysenmethode.

In Zusammenarbeit mit: BÖHLER EDELSTAHL

Improvement of the Characterisation of Nonmetallic Inclusions Especially Focusing on High Purity Steels for Aeronautic Applications

Master Thesis
submitted by

Susanne Penz

Abstract

Due to the constantly increasing requirements for steels applied in the aerospace industry, a reliable characterisation of nonmetallic inclusions steadily gains importance. Out of the different described methods for inclusion analysis, the focus of this thesis lies on automated SEM/EDX investigations. On the basis of first analyses, an inclusion cluster consisting of 25 different inclusion classes especially adapted to the steel grade PH 13-8 Mo is developed which permits an inclusion categorisation over the whole process flow. Next to the comparison with a similar analysing method (P-SEM) and the variation of several influential parameters, the representativeness of this method and the applicability of the inclusion cluster on a different steel grade is tested. The results underline the potential of this analysing method.

In cooperation with: BÖHLER EDELSTAHL

Acknowledgements

First and foremost, I would like to thank my thesis advisor Dipl.-Ing. Susanne Linzbacher for her continuous support and her helpful suggestions during the completion of this work.

Moreover, special thanks goes to Univ.Prof. Dipl.-Ing. Dr.mont. Wilfried Krieger for his efforts and to all members of the *Chair of Metallurgy* for their assistance.

Furthermore, I would like to thank Dipl.-Ing. Ronald Hasenhündl and the whole R&D–team of Böhler Edelstahl GmbH for the excellent cooperation, the interesting discussions and the constructive comments.

Lastly, I thankfully appreciate the patience and encouragement of my family during the years of my study and the time of the preparation of this thesis.

Affidavit

I hereby declare that the following diploma thesis has been written only by the undersigned and without any assistance from third parties.

Furthermore, I confirm that no sources have been used in the preparation of this thesis other than those indicated in the thesis itself.

Susanne K. Penz

Leoben, June 2007

Contents

List of Figures

List of Tables

List of Acronyms

BSE	Back Scattered Electrons
CT	Computer Tomography
CBCT	Cone Beam Computer Tomography
ECD	Equivalent Circle Diameter
EDX	Energy Dispersive X-ray
EPMA	Electron Probe Micro Analysis
FET	Field Effect Transistor
OES-PDA	Optical Emission Spectrometry with Pulse Discrimination Analysis
PE	Primary Electrons
PH	Precipitation Hardened
PREN	Pitting Resistance Equivalent Nitrogen
P-SEM	Personal Scanning Electron Microscope
SE	Secondary Electrons
SEM	Scanning Electron Microscope
VAR	Vacuum Arc Remelting
VIDP	Vacuum Induction Degassing and Pouring
VIM	Vacuum Induction Melting
WDX	Wavelength Dispersive X-ray

List of Symbols

A	Feature area, μm^2
A_5	Elongation after fracture, %
c_{Fe}	Concentration of iron in the matrix, $wt.$-%
c_i	Concentration of element i in the matrix, $wt.$-%
RA	Reduction of Area, %
R_m	Ultimate tensile strength, MPa
$R_{p_{0.2}}$	Yield strength, MPa
x_{Fe}	Concentration of iron in particle, $wt.$-%
x_i	Concentration of element i in particle, $wt.$-%

1 Introduction

The requirements for steels applied in the aerospace industry – especially as far as micro cleanliness is concerned – increase constantly. The challenge not only consists in fabricating these steel grades, but also in the selection of an appropriate method for inclusion characterisation, since the methods are just as manifold as the origin and the nature of inclusions.

The fundamental question of inclusion analysis is that of representativeness, given the often relatively small analysed sample volume. Jacobi [1] refers to this given difficulty with the statement, *"Clean steel is harder to measure than to produce"*. Therefore the essential responsibility is to decide for a method accordant to the particular application and to examine the obtained results with the required accuracy.

In the first part of this thesis a literature review on the analysed material (PH 13-8 Mo) – a precipitation hardenable martensitic stainless steel – together with the theoretical basics on inclusion formation and classification are presented. Secondly general problems for the inclusion characterisation and different methods for the analysis of micro cleanliness are described in order to get an impression of the huge spectrum of possibilities including the advantages and disadvantages as well as the application limits of each method. Furthermore the differentiation between common and automated methods is illustrated especially regarding the aspect of representativeness.

In the practical part the cleanliness of steel samples is investigated by an automated SEM/EDX analysis. Two different types of analysing equipments are used: Firstly the INCA system installed at the Chair of Metallurgy at the University of Leoben, and secondly the Personal Scanning Electron Microscope (P-SEM) applied at voestalpine Stahl GmbH in Linz. Within the scope of the practical work, an offline evaluation system is adapted to the analysed steel grade PH 13-8 Mo including an especially defined inclusion cluster. Moreover several influential parameters on SEM/EDX investigations used for inclusion analysis are discussed and a comparison between the results of INCA and P-SEM is carried out. Finally the practical part is completed by the analysis of four samples of the same melt taken at different process steps in order to get an insight into the inclusion development and modification in the course of the process.

2 The Material: PH 13-8 Mo

2.1 General Properties

The PH 13-8 Mo (X3CrNiMoAl13-8-2) is a precipitation hardenable martensitic steel. Combining the properties of maraging steels with those of stainless steels, it is particularly applied in the aviation industry. Maraging steels were developed in the 1960's for applications requiring high strength in combination with good fracture toughness. They are characterised by a low carbon content and Ni-contents up to 19 *wt.*-%, as well as substantial amounts of Co and Mo together with small additions of Ti. A modification of this basic alloying concept, depending on the specific applicatory requirements, is possible. In the case of the PH 13-8 Mo, an improved corrosion resistance is required, wherefore great amounts of Ni are replaced by Cr [2].

Stainless steels are characterised by a corrosion resistance against gases, aqueous solutions and acids. The basic demand to this group of steels is a preferably limited and constant area attack in combination with a resistance against local limited corrosion defects. Furthermore adequate strength and ductility, also under thermal or dynamic strain, as well as plasticity and weldability are ranked among important material properties [3].

2.1.1 Position in the Group of Stainless Steels

Stainless steels can be classified in different types, according to their microstructure:

- ferritic steels
- martensitic steels
- austenitic steels
- ferritic-austenitic steels

This classification is illustrated in the so-called Schäffler diagram, giving a general overview on the dependency of microstructure formation and chemical composition, as shown in **Fig. 2-1**, where the position of PH 13-8 Mo is marked with a red dot.

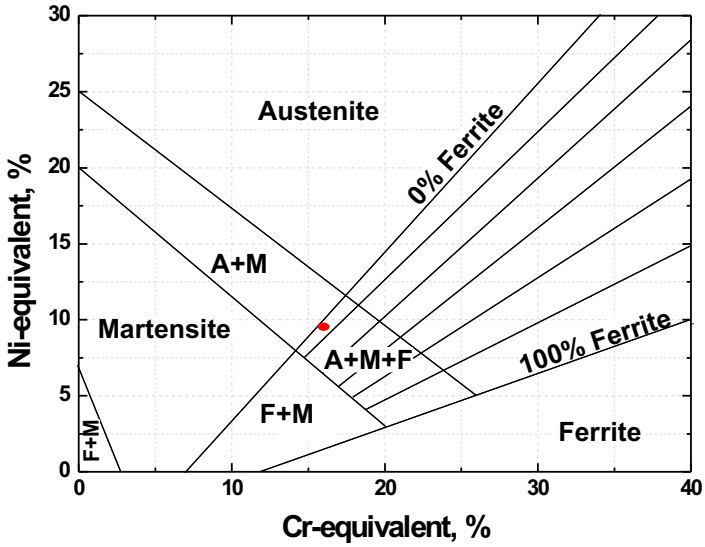

Figure 2-1: *Schäffler diagram [4].*

Regarding **Fig. 2-1**, it can be seen that the microstructure formation is basically dependent on the so-called Cr- and Ni-equivalents. This results from the fact that alloying elements either stabilize the ferritic α or the austenitic γ-phase. Whilst elements like Cr, Al, Ti, Si, Mo and P enlarge the α-zone in the Fe-Fe_3C diagram, the elements Ni, C, N, Co and Mn expand the austenite. The effects of Cr and Ni on the phase diagram are illustrated in **Fig. 2-2**. Therefore the effect of these two groups of elements can be summarised as described in **Eqs. (2-1)** and **(2-2)** [4]:

$$Cr\text{-equiv.} = \%\,\mathrm{Cr} + 1.4\ wt.\text{-}\%\,\mathrm{Mo} + 0.5\ wt.\text{-}\%\,\mathrm{Nb} + 1.5\ wt.\text{-}\%\,\mathrm{Si} + 2\ wt.\text{-}\%\,\mathrm{Ti} \quad (2\text{-}1)$$

$$Ni\text{-equiv.} = \%\,\mathrm{Ni} + 30\ wt.\text{-}\%\,\mathrm{C} + 0.5\ wt.\text{-}\%\,\mathrm{Mn} + 30\ wt.\text{-}\%\,\mathrm{N} \quad (2\text{-}2)$$

Originally the Schäffler diagram was plotted for melted weld material of Cr-Ni steels in quenched condition. Therefore, Brezina [6] states that the validity of this diagram is limited regarding cast and forged material. According to the diagram pure martensite can theoretically exist up to a Cr-equivalent of approximately 15 $wt.$-% and a Ni-equivalent of 8.8 $wt.$-%. In practice, certain types of martensitic steels without ferrite or residual austenite

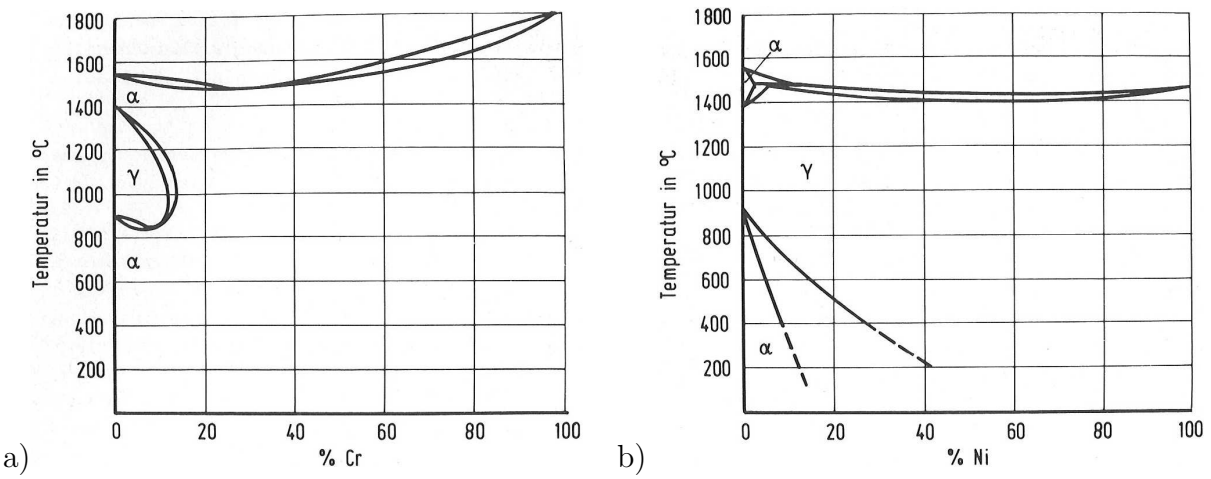

Figure 2-2: *a) Binary Fe-Cr system with constricted γ-field and b) Binary Fe-Ni system with open-γ field [5].*

exist, which are not situated in the martensite field of the Schäffler diagram (e. g. PH 14-5). Moreover Brezina [6] demonstrates that in this diagram an equivalence between high C- and Ni-contents exists. He exemplifies this context on the basis of two different steels, one with a high Ni-content, the other with a high carbon content. Their position on the diagram overlaps, although the steel with a high Ni-content, in contrast to the other one, builds fine dispersive austenite stable down to room temperature, after tempering at 600 ℃. A fact, which the Schäffler diagram cannot represent [6].

Seetharaman *et al.* [7] state an analogous indication concerning the PH 13-8 Mo. According to the Schäffler diagram, this steel should contain a mixture of austenite and martensite at room temperature. Based on simple calculations for estimating martensite start temperature, a complete transformation to martensite during cooling to room temperature can be expected. Because of this Seetharaman *et al.* note that a prediction of the occurrence of different phases with the aid of the Schäffler diagram is only reasonable for samples which have undergone a thermal history similar to that of weld material [7].

2.1.2 Alloying Concept

Tab. 2-1 shows an average chemical composition of a PH 13-8 Mo. In the following the effect of the most important alloying elements is discussed.

Table 2-1: *Chemical composition of PH 13-8 Mo in wt.-% [8].*

% C	% Si	% Mn	% Cr	% Mo	% Ni	% Al
0.03	< 0.08	< 0.08	12.70	2.20	8.10	1.1

Cr: The most important alloying element for stainless steels is Chromium. The corrosion resistance of steels is based on the formation of a passive film at the surface because of an electrochemical reaction. This crystalline film, being only a few *nm* thick, is composed of metal oxides and metal hydroxides. An increasing Cr-content enhances the development of an amorphous, dense passive film, since Cr lowers the passive and the passivating current density and thereby enhances steel passivation. Corrosion resistance is generally assured by adding at least 12 *wt.*-% Cr. However only the free Cr-content is decisive for the corrosion behaviour, meaning the amount of Cr not bonded to e. g. C or N. Since a certain percentage of Cr is often bonded in form of carbides, the free Cr-content can therefore be lower than the overall Cr-content [4].

Mo: Molybdenum in its appearance as α-stabilizer also enhances the resistance against corrosive media, particulary against pitting, meaning a localised corrosion at individual sites on the surface of stainless steel starting at weaknesses in the protective oxide film. An indication of the material's pitting corrosion resistance is given by the "Pitting Resistance Equivalent Nitrogen" (PREN) number as shown in **Eq. (2-3)** [4]:

$$\text{PREN} = wt.\text{-}\%\,\text{Cr} + 3.3\ wt.\text{-}\%\,\text{Mo} + (16 - 30)\ wt.\text{-}\%\,\text{N} \tag{2-3}$$

The higher this factor the better is the corrosion resistance. In practice values up to 40 can be reached for PREN. Molybdenum additionally increases high-temperature strength and hardenability.

Ni: Nickel is – next to Cr – the most important alloying element in stainless steels. It is a γ-stabilizing element and improves the overall corrosion resistance in acids, especially against stress corrosion cracking. It enables the martensite formation at reduced carbon contents, resulting in so called Ni-martensites. These steels are characterised by a considerably better ductility than common martensitic steels, also in thick-walled sections [3].

C: Carbon is a very strong γ-stabilizer and an essential component of all steels. From the point of view of corrosion, C-contents should be as low as possible [4], in order to avoid bonding of Cr. Owing to the low carbon content (< 0.05 $wt.$-%), Ni-martensitic steels feature good weldability, provided some aspects regarding martensite transformation and the thereof resulting residual stress, distortion and cracks are considered.

Al: Aluminium is used for precipitation hardening. Details are discussed in section 2.2.

Si: Silicon particulary improves scale resistance and corrosive behavior in highly concentrated HNO_3.

Mn: Manganese does not have an noticeable effect on the corrosion resistance [3].

2.1.3 Mechanical and Physical Properties

The properties of martensitic chromium steels, which have a significantly higher hardness and strength than all other stainless steels, are highly affected by microstructure which is again influenced by the heat treatment. For this reason the properties vary in a wide range, between more or less tempered martensite and precipitated carbides. With increasing tempering temperature carbides with high Cr-content precipitate, whereby the mixed crystal becomes poorer in corrosion resistant Chromium [3]. **Tab. 2-2** shows an overview of the mechanical properties of PH 13-8 Mo at room temperature [8]

Table 2-2: *Mechanical properties PH 13-8 Mo at room temperature [8].*

Condition	Hardness HRC	$R_{p0.2}$ MPa	R_m MPa	A_5 %	RA %	Impact strength at 20 ℃ J
Solution Annealed	< 38	–	–	–	–	
PH I*	$40 - 45$	1140	1210	12	50	54
PH II	$43 - 48$	1310	1410	9	50	40
PH III	$45 - 50$	1410	1520	9	45	32

*PH: precipitation hardened

According to Brezina [6], low strength grades are used in most applications. As a reason, the author states the risks when fabricating very large components (crack formation, distortion, etc.). These facts are not balanced by the significantly better properties as far as erosion resistance and fatigue strength are concerned. Moreover especially minimised risk of stress corrosion cracking is characteristic for grades of lower strength. As already discussed ductility rises with increasing Ni-content. Therefore an application is possible at deep temperatures as a result of the low transition temperature [6].

In **Tab. 2-3** an overview of the physical properties at room temperature of the PH 13-8 Mo is illustrated [8].

Table 2-3: *Physical properties of PH 13-8 Mo at room temperature [8].*

Density $kg\,m^{-3}$	Young's Modulus MPa	Th. expansion 20 ℃–100 ℃ K^{-1}	Th. conductivity at 100 ℃ $W\,m^{-1}K^{-1}$
7.74	202×10^3	10.5×10^{-6}	14

2.1.3.1 Influencing Variables on Microstructure

Various investigations have been made in order to characterise the microstructure of the PH 13-8 Mo during solidification and heat treatment. According to results of Differential Thermal Analysis (DTA) and high-temperature water-quench experiments made by Cieslak *et al.* [9], the typical microstructure of PH 13-8 Mo at room temperature is martensite with residual δ-ferrite, which is enriched in Cr. The presence of residual δ indicates that not enough time was available at a given cooling rate to allow a complete δ-γ transformation. Based on their DTA results, the authors assume that the δ-γ transformation is quench-rate sensitive; lower solidification and cooling rates will result in a smaller amount of retained δ, even though the solidification structure is coarser. Hence they conclude that larger castings of PH 13-8 Mo may be nearly δ free in comparison to more rapidly solidified structures [9].

Thermal and mechanical stability of austenite in PH 13-8 Mo as a function of aging temperature and time was studied by Garrison and Brooks [10]. They observed an embrittlement coincident with precipitation hardening. There are several possible reasons which

are suggested to contribute to this behaviour. In additon to the precipitates themselves and the precipitaion of a chromium rich phase at 475 ℃ after long time aging as possible explanations, the decomposition of retained austenite is one of the possible mechanisms of embrittlement. This decomposition and the resulting precipitation of carbides at interfaces can cause changes in the mechanical stability of austenite. The study focused on the determination of the amount of austenite in PH 13-8 Mo as a function of aging temperature of time. No retained austenite was found in X-ray measurements during tempering, wherefore it is suggested that the described embrittlement is not related to the decomposition of austenite [10]. The other possibilities were neither confirmed nor denied.

Several publications concerning PH 13-8 Mo deal with the formation and growth of cracks and the failure behaviour of critical parts [11, 12, 13]. The failure of two aircraft components, one from a landing gear, the other from an ejector rack mechanism, made from PH 13-8 Mo was investigated in [11]. Sub-surface initiation of numerous cracks with a wide range of orientations and cleavage like features were identified to be the first stage of both failures. Hydrogen embrittlement was identified to be the most likely mechanism for initial crack growth. According to Roth *et al.* [11], the resistance against hydrogen-assisted-cracking will increase with higher aging temperatures. However this would be connected with a reduction in the tensile strength and therefore is not recommended.

2.2 Theoretical Background

2.2.1 Precipitation Hardening of PH 13-8 Mo

Ni-martensites are especially apt for precipitation hardening through intermetallic compounds in the temperature range from 450 to 600 ℃. The best hardening effects are reached in combination with Titanium, followed by Aluminium, Copper, Niobium and Molybdenum [14]. In the following the general precipitations mechanisms are illustrated.

2.2.1.1 Precipitation Mechanisms

When treating precipitation hardening two strengthening mechanisms have be considered: Firstly the so-called Orowan mechanism and secondly the shearing mechanism. Whilst the former implies that incoherent particles overcome hindrances through bypassing, leaving back a ring at the dislocation, the latter means that a particle is sheared through a coherent precipitation. General details are explained in [15], their specialities regarding the PH 13-8 Mo are treated in Seethamaran *et al.* [7]:

According to the authors, the Orowan mechanism can not be responsible for strengthening in the case of aged samples of PH 13-8 Mo. Aging the martensite in the temperature range between 450 and 575 ℃ leads to finely distributed spherical particles of NiAl precipitates, which remain fully coherent with the matrix even after considerable coarsening provided that the aging was carried out at temperatures below 525 ℃. The low constrained lattice mismatch between the precipitates and the matrix is mentioned as a possible reason for this effect. Therefore the authors conclude that the operative strengthening mechanism involves the shearing of the NiAl precipitates. When aging at temperatures higher than 525 ℃, significant amounts of particles of residual austenite form, which coarsen very rapidly. Additionally a resulting decrease in strength at higher temperatures is also observed in [16]. The authors attribute this phenomenon to the formation of larger carbides and residual austenite. This relation is illustrated in **Fig. 2-3** where it is also compared to two other steels.

in **Fig. 2-4** Ping [16] also points out that the Orowan mechanism is not responsible for hardening in the case of PH 13-8 Mo. This would indicate that the peak hardness appeared at the highest precipitate density (i. e. consequently the shortest inter-particle distance). Investigations show that the hardness increases as the NiAl particles grow. Therefore the hardening effect can be explained by the shearing mechanism.

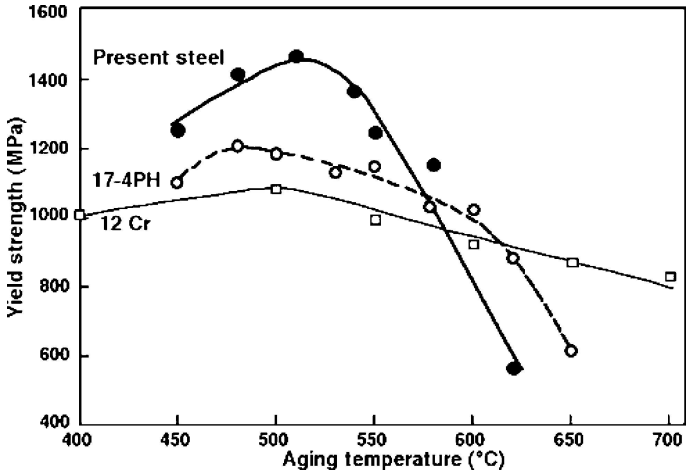

Figure 2-3: *Variation of yield strength behaviour in PH 13-8 Mo with annealing temperature [16].*

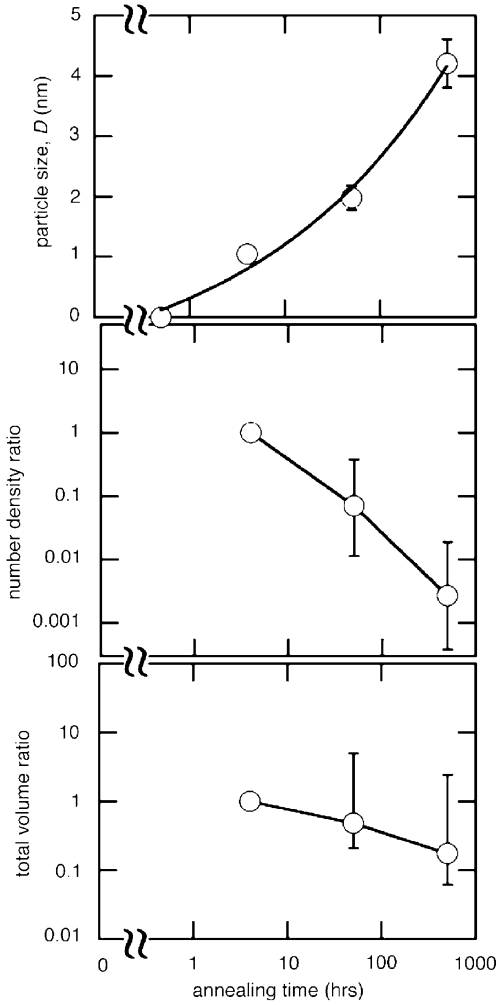

Figure 2-4: *Average precipitate size, number of density ratio and total volume ratio as a function of aging time at 450 °C [16].*

2.2.1.2 Growth and Structure of NiAl Precipitates

Seetharaman *et al.* [7] demonstrate that the growth of NiAl precipitates generally involves three stages:

- The appearance of solute-rich clusters or Guinier-Preston zones,
- the formation of finely distributed transition phases coherent with the matrix,
- the emergence of coarse and incoherent precipitates of equilibrium composition.

While the peak value of the yield strength of the alloy is achieved in the first or second stage, the last stage is characterised by a considerable softening of the alloy due to overaging. According to Ping [16] the size and concentration of precipitates increases simultaneously with increasing annealing temperature, while a decrease in number can be observed.

As already discussed, PH 13-8 Mo is strengthened on aging by precipitation of the intermetallic $\beta-$NiAl, built up by an ordered cubic B2 crystal structure (CsCl), which is based on two interpenetrating primitive cubic cells. While the Aluminium atoms occupy the corners of the first sublattice, the cube corners of the second sublattice are occupied by Nickel atoms [17]. This theory is also confirmed by Guo and Sha [18] who used thermodynamic calculations for the quantification of phase fractions and element participation in precipitation hardening steels, among them also the PH 13-8 Mo.

Numerous investigations have empirically analysed the kinetics of precipitation in maraging steels through application of the Johnson-Mehl-Avrami equation, which can be used to describe the progress of a large number of nucleation and growth reactions. Details are again illustrated in [15]. Robino *et al.* [19] have found that the Avrami formalism does not provide a full description of the precipitation kinetics of the PH 13-8 Mo. Consequently some sources of errors must be considered. According to them the recovery and reversion of martensite to austenite cannot be neglected in regarding the hardening kinetics. But it is important to note that the Avrami analysis presents an useful methodology for an evaluation of the hardening response of PH 13-8 Mo.

2.2.1.3 Other Hardening Mechanisms

Although precipitation hardening is definitely the most important effect, it is not the only decisive mechanism for the strength of maraging steels. The combination of different mechanisms like mixed crystal-, dislocation-, particle- and grain boundary hardening are utilised systematically [14] – Almeida and Ribeiro [20] have, for example, studied the relationship between mechanical properties and microstructure for the PH 13-8 Mo with the objective of characterising the nature of precipitations. Solution treated material and after aging samples at different temperatures were investigated, whereby carbides were identified in both conditions. Furthermore peaks of carbide forming elements in the lath boundaries were identified by Scanning Electron Microscopy. According to [20], carbide precipitation characteristics additionally affect the toughness of the PH 13-8 Mo.

2.3 Application and Fabrication

Owing to its remarkable resistance to stress corrosion cracking and the high strength until 315 ℃, the PH 13-8 Mo is particulary used for applications in the aerospace industry: high strength screws, bolts and landing gear parts. Furthermore the steel is used in the petrochemical industry and for nuclear reactor components. In order to ensure the micro cleanliness which is critical for the high fracture toughness of safety components, the vacuum technology is essential. Consequently the PH 13-8 Mo is produced through a double melting process. It is melted under vacuum and further remelted in the vacuum arc furnace after solution annealing. Subsequently heat treatment and rolling processes together with cooling under air complete the production route [8, 21].

2.3.1 Vacuum Induction Melting (VIM)

The VIM operates on the same principle as conventional induction melting does. Electromagnetic induction is melting the metal by inducing eddy currents resulting from an external

alternating current coil. Since the adjustable process parameter such as pressure and temperature greatly influence the resulting melt, a preferably efficient treatment is possible.

Next to an unproblematic selective alloying of escharotic elements, low carbon and gas contents, the VIM allows a reduction of nonmetallic inclusions and contents of detrimental accompanying elements to a minimum. When treating trace elements such as Pb, Bi, Se or Te – which affect the durability of critical parts – the VIM proves especially useful. Because of the relatively high vapour pressure of these elements, vacuum conditioning allows an effective reduction. Hydrogen and Nitrogen can also dissipate through the gas phase following Sieverts' law. On the other hand, the decrease of nitrogen, can be hindered or even averted in presence of nitride building elements like Cr, V, Al or Ti. Apart from these mostly pressure-dependent reactions, interactions between melt-slag and refractory coating must be considered. It has been observed that the specific bath movement in the VIM leads to a formation of incrustations on the crucible border, whereby the slag-bath reactions is impeded and an increased refractory wear is observed. Therefore a slag free handling has been established. In return desulfurisation is difficult in the VIM since a Calcium treatment under reduced pressure is even more difficult than under atmosphere. Hence it is recommended to use starting material with very low sulphur contents.

Today the so called Vacuum Induction Degassing and Pouring (VIDP)-furnace is used. In comparison to a conventional VIM, the VIDP itself is vacuum-sealed and does not have an extra vacuum chamber, which results in smaller volume that must be evacuated. The melt is tapped through a launder tundish system, which supports the separation of nonmetallic inclusions [22].

2.3.2 Vacuum Arc Remelting (VAR)

Basically, the energy needed for remelting the ingot is transferred by an arc which ignites between the melting ingot or electrode (cathode) and the melt pool (anode). Small metal drops dissolve from the electrode and are absorbed in the liquid pool inside a water cooled crucible. A schematic illustration of the procedures during remelting is given in **Fig. 2-5**.

This remelting process especially improves the purity and the ingot structure. The contents of trace elements and dissolved gases can be minimised. Furthermore a highly uniform distribution of remaining inclusions, virtually isotropic properties and optimal polishability can be reached [22].

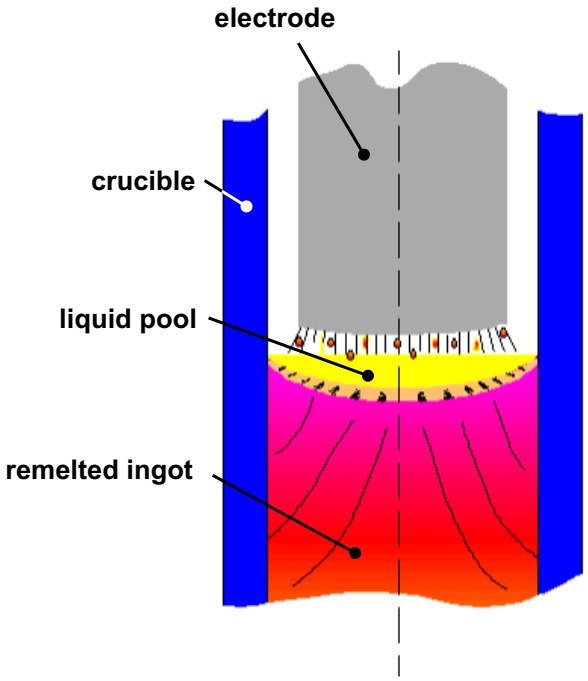

Figure 2-5: *Schematic illustration of the VAR process [23].*

3 Inclusions

3.1 Classification

3.1.1 Definition

Basically a certain number of inclusions is present in every finished steel product. The composition of inclusions is different to the surrounding matrix with which they build up a defined phase boundary. Generally distinctions between inclusions with metallic and those with nonmetallic character have to be made [24]. Inclusions which do not come from the steel melt itself are called exogenous. They mostly consist of molten or carried along smallest particles from the lining (nonmetallic inclusions) or not dissolved residues of alloying elements (metallic inclusions). The appearance of exogenous inclusions is relatively rare. In contrast to this, nonmetallic endogenous inclusions, which are the product of metallurgical reactions in the melt, occur more frequently. Thereby either deoxidation products like oxides or compositions of steel accompanying elements like for example sulfides or carbonitrides are affected. Both types influence the properties of steel: while endogenous inclusions are relatively small and distributed constantly in the majority of cases, exogenous types are comparatively large and irregularly spread [25].

3.1.2 Classification Criteria

According to Dahl [24], inclusions can be classified on the basis of four criteria: size, origin, cause of formation and composition.

The size of inclusions – varying in a wide range between less than 1 μm and some 100 μm – is one of the most essential factors, which influences the properties of the finished product as well as the possibilities of inclusion detection and characterisation [26]. More detail is given in chapter 4.

According to their time of emergence, inclusions can be classified in four categories [27]:

- Primary inclusions, which form in the melt immediately after addition of the deoxidant,
- secondary inclusions, which emerge while cooling to liquid temperature,
- tertiary inclusions, which occur between liquid and solid temperature ,
- quaternary inclusions, which appear in the solidified state.

According to [27], precipitation of inclusions is possible in the solid state too, because the solubility of the matrix for deoxidation media as well as oxygen decreases further with falling temperature. As already mentioned, the cause of formation can be exogenous or endogenous. As far as the composition of non metallic inclusions is concerned, the following types can be differentiated: Oxides, Sulfides, Nitrides, Carbides and hybrid forms. In general oxides are most important regarding cleanliness [24].

3.2 Formation

3.2.1 Kinetic Basics

In the following an overview of the physical procedures for the formation and separation of nonmetallic inclusions is discussed. Further details are given in [25].

3.2.1.1 Nucleation

Generally, two mechanisms for nucleation exist: homogeneous and heterogeneous. Principally a homogenous phase is characterised by a defined temperature and composition. This phase can get thermodynamically instable, if one or both of the influence parameters change resulting in the formation of nuclei if the critical enthalpy of formation is transgressed. This causes the formation of a heterogenous phase mixture. The incipient process is called homogenous nucleation.

A heterogenous nucleation however occurs, if the new phase forms on an already existant foreign nuclei. This can, for instance, be the crucible wall, impurities in the melt or deoxidation products of different types, which have emerged before.

The driving force for the formation of a new phase is a supersaturation, which is characterised by the difference between the free enthalpy of the initial system and the final system [25].

Supersaturation can be the cause of segregation during solidification. In general, two models for describing the segregation of nonmetallic inclusions during solidification exist [24]:

Model for the rhythmic precipitation of inclusions

Nucleation is necessary for building a new phase at the solidification front, whereby the formation of solid or liquid nonmetallic inclusions partly inhibits the nucleation process. Since the emerging inclusions have a remarkable interfacial energy to the liquid phase, the necessary nucleation force for homogenous nucleation is accordingly higher. Therefore nucleation can only take place at high supersaturations. Several segregation models show that the maximum supersaturation is found directly at the solidification front.

Inclusion precipitation at the grain boundaries

If the condition of an critical supersaturation is not fulfilled as descried in the first model, nucleation cannot take place. It is assumed that in this case, supersaturation is reached through two, on each other tapering, solidification fronts. This causes an addition of the concentration enrichments ahead of the fronts.

3.2.1.2 Growth Mechanisms

Deoxidation is seen as one of the main causes for the formation of nonmetallic inclusions. Because of this the growth mechanisms are described on the basis of the growth of deoxidation products. Growth and separation of deoxidation products are closely connected and occur in parallel. **Fig. 3-1** shows the schematic procedures during a typical deoxidation process.

Microbial growth through diffusion is the decisive factor in the initial period, as long as a supersaturation is present. A theoretical final point is reached by obtaining equilibrium

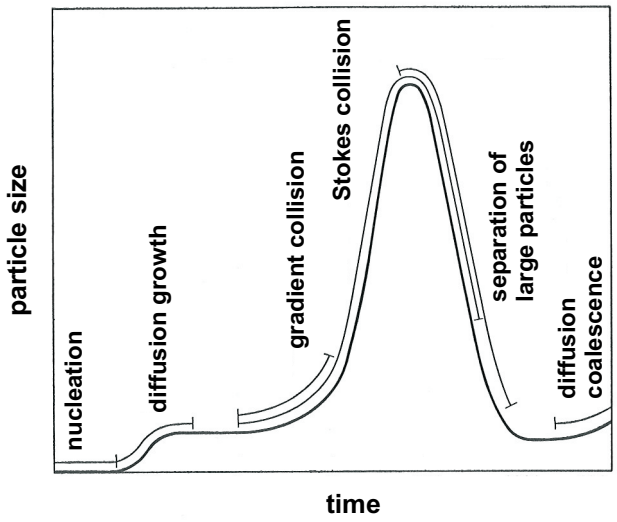

Figure 3-1: *Schematic procedures during a typical deoxidation process [25].*

concentration. The coalescence of deoxidation products by increasing the surface energy is called coagulation. Collision growth is based on compact particles which collide accidentally, while they are moving in the steel melt with different velocities or directions. They can adhere together, provided the necessary interface condition is given. Generally, a distinction between gradient collision, where natural or forced flows lead to velocity gradients and Stokes collision is made. In the latter case it is assumed that particles of different size and density ascend differently quick and that larger particles can catch smaller ones. Finally, diffusion coalescence – also known as Ostwald Reifung – where larger particles grow at the cost of smaller ones at sufficiently long deoxidation times, occurs. It must be added that all these mechanisms can partly interfere with each other. The influence of the Brownian motion on the growth of nonmetallic inclusions is marginal [25].

3.2.1.3 Separation

Regarding the separation of nonmetallic inclusions from the steel melt some influencing factors have to be considered. Essential parameters are the properties of the particles like size, density and state. Furthermore growth velocity, stream ratios in the steel bath as well as the material of the refractory lining and slag covers are decisive. Specific explanations of these coherences are explained in [25].

3.3 Influence on Steel Properties

Principally a high content of nonmetallic inclusions in the finished product is undesirable, whereby nature, size, form and distribution of inclusions are of particular importance. These properties are highly influenced by the chemical composition of liquid steel. Owing to their marginal coherence with the matrix, they often cause material failures. On the other hand inclusions can also have a positive effect. They can, for instance, serve as seed crystals in the solid steel and are hence advantageous for primary or secondary crystallisation. Moreover inclusions are used in special steel grades for enhancing the grindability of, e. g., free cutting steels. Regarding the inclusion distribution it becomes apparent that a large local concentration has negative consequences on material properties such as impact strength, fracture toughness or fatigue resistance and should be avoided as far as possible [25].

Consequently it is important to have a possibility for analysing the inclusion landscape in order to prevent material failure. Moreover analysing methods decisively contribute to the further development of highly clean steels, as described in the next chapters.

4 Common Analysing Methods for Nonmetallic Inclusions

Various methods for the characterisation of nonmetallic inclusions exist. In the following several of the most common and important methods for practical use and also the associated problems are described.

4.1 General Problems when Characterising Inclusions

As a result of the constant improvement of secondary metallurgy, cleanliness of steels was improved considerably. This makes the inspection of inclusions difficult. According to Angeli [26], inclusions are divided into four size categories:

- macro inclusions ($> 100\ \mu m$)
- meso inclusions ($>\ 30\ \mu m$ and $<\ 100\ \mu m$)
- micro inclusions ($>\ 1\ \mu m$ and $<\ 30\ \mu m$)
- submicro inclusions ($< 1\ \mu m$)

A size distribution curve of inclusions is basically applicable for describing the cleanliness of steels. The macro cleanliness has reached a relatively high qualitative level in recent years. Therefore statistical problems arise for the characterisation of macro inclusions, since they are coincidentally distributed in the steel matrix and their frequency of occurrence is rather low. The number of inclusions per unit area, respectively per volume, certainly depends on the steel grade and the process chain. Due to their irregular appearance, the identification of macro inclusions in pure steel qualities is often very difficult. According to Angeli [26] the probability for finding large inclusions is therefore one of the most important criteria regarding cleanliness. This difficulty is described in **Fig. 4-1**.

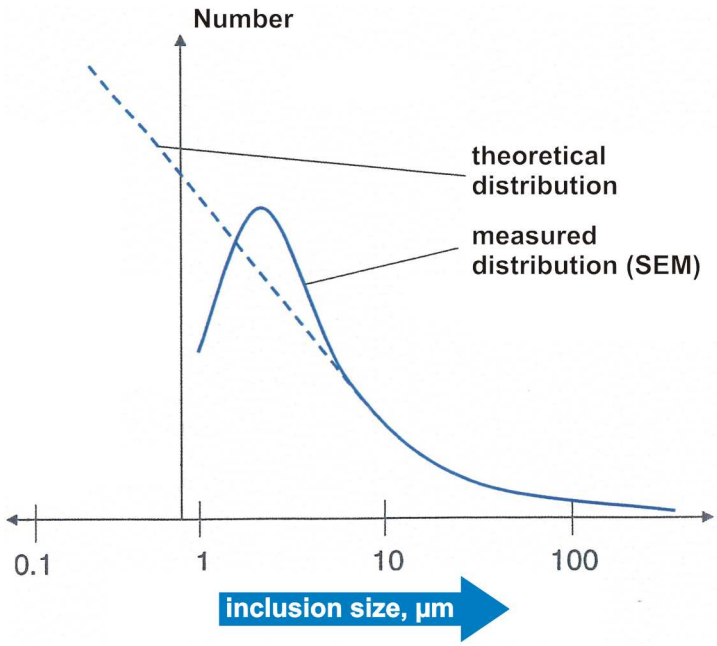

Figure 4-1: *Size complexity for inclusion characterisation [26].*

Micro inclusions however are arbitrarily frequent. Locating them and the subsequently resulting evaluation of the microscopic cleanliness is less complicated for a qualitative analysis. Conversely the problem lies in the detection of inclusions in the submicroscopic area. There the possibility of partly reaching the resolution limit of the respective method exists [26].

A critical inclusion size, above which inclusions are hazardous and can cause the failure of steel products, is frequently defined. Atkinson [29] states that this critical size can be estimated using fracture toughness calculations, provided that inclusions can be regarded as defects similar to cracks in the steel matrix. It must be added that the critical size varies for different properties of steels, for example, fatigue, welding, bend fracture strength, hot working and corrosion [29].

Next to the described problems, there are other influencing factors which have to be considered regarding inclusion characterisation. An example therefor is the formability of inclusions. If a dilation of inclusions occurs during the forming process of semi-finished products, this could contribute to a falsification of investigations. Consequently a defined size classification based on a 2-dimensional view is often difficult [30].

Due to all these discussed influences, the general problem of representativeness arises. Owing to the low incidence of inclusions and limited testing volumes of most cleanliness assessment methods, the measured result strongly depends on the sampling. The examination of unrealistically large areas or volumes is required to give a statistically significant measure of the inclusion content. This often proves as very extensive and therefore uneconomic [29, 30].

The focus of this thesis lies on the methods of characterisation of micro inclusions. As far as methods of characterisation for macro inclusions are concerned, the reader is referred to [31, 32], since macro inclusions are not relevant in this thesis.

4.2 Standard Chart Comparison

This method has been the traditional approach for rating inclusion contents of steels. It describes the inspection of nonmetallic inclusions in the form of oxides and sulfides in special steels. Given that defined preconditions are applied, these norms can also be used for characterising other steel grades. In general, the identification and classification of inclusions is achieved by comparison with charts.

Although Standard Chart Comparison is relatively quick and facile, it should be noted that nitrides and carbides are not considered. Moreover less quantitative information about the size and morphology of inclusions is given than with an image analysis system [26]. In the following the two most frequently applied standards for chart comparison are listed.

4.2.1 DIN 50 602

This norm differentiates between the following classes:

- SS: sulfides in streak form
- OA: dissolved oxides (Alumina)
- OS: oxides in streak form (Silica)
- OG: globular oxides

For the determination of cleanliness two different methodologies exist: The first being Method M where only the maximum inclusion size of the different types is identified. With the latter being method K, the inclusion content in the sample is determined through summing up all inclusions and multiplying them with a given quantifier. The reproduction scale is 100 : 1. **Fig. 4-2** illustrates part of the afore mentioned comparison chart.

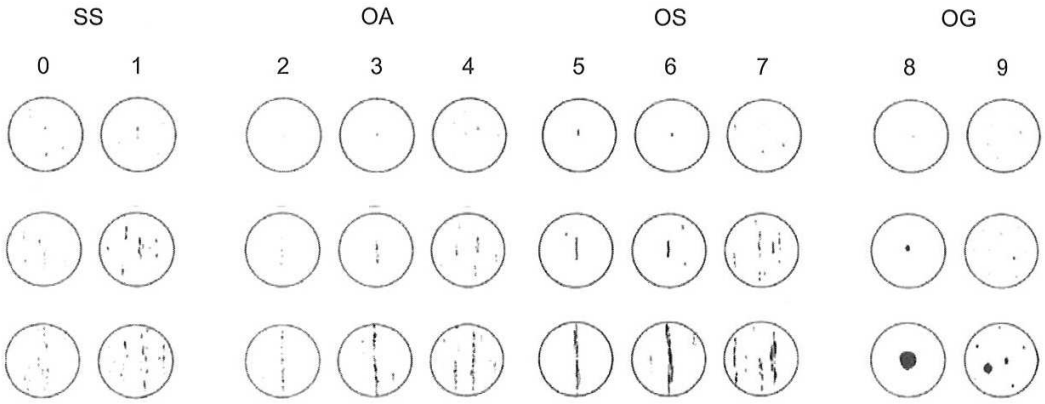

Figure 4-2: *Extract of a comparison chart [28].*

In the chart, the size of the analysed inclusions increases from figure 0 to figure 9, whereby the last can partly represent even macroscopic inclusions. The surface area duplicates from chart to chart according to the geometric series 2^n, where n signifies the figure size.

The samples are examined under the optical microscope with a magnification of 100×. The observation field must have the same size as the comparison charts (preferably 80 mm diameter). In general at least six samples with a minimum area of 100 mm^2 are inspected. When preparing the samples, special attention has to be paid so that the inclusions are not torn out of the matrix. Moreover an infiltration of grinding material in the sample surface should be avoided. The hence evaluated cleanliness is referred to an area of 1000 mm^2 [33].

4.2.2 ASTM E 45

In general this norm is very similar to the DIN 50 602. A distinction between three categories named Plate I, Plate II and Plate III is made. Plate I is categorised in the following four types:

- A: sulfides
- B: dissolved oxides
- C: oxides in streak form
- D: globular oxides

Each of these groups is divided into a thin and heavy series and additionally in five lines, describing the length of the inclusions for types B and C and the frequency of the inclusions for types A and D respectively. In contrast to Plate I, Plate II is only split into two groups (oxides in streak form and dissolved oxides) – sulfides are not considered. Plate III is similar to Plate I and only differs as far as the sectioning in lines is concerned. Every line is again divided in half-steps. This plate is especially applied for steels which are melted under vacuum.

Similar to DIN 50 602 different methodologies exist for the determination of cleanliness: Method A – which is applied most frequently – uses Plate I and identifies the maximum size of each inclusion type on the sample. In order to avoid the lengthwise cutting of inclusions, the samples have to be taken parallel to the forming direction [34].

4.3 OES-PDA

Optical Emission Spectrometry with Pulse Discrimination Analysis (OES-PDA) is currently the fastest method for inclusion characterisation. In less than 10 minutes, inclusions and inhomogeneities smaller than 12 μm are detected. Modern equipments are able to identify nearly all elements of the periodic system (PSE) within a few minutes. However OES-PDA cannot provide any morphological data of the inclusions [35].

Although the depth of penetration with about 1 μm is comparatively small, the significance of OES-PDA concerning inclusion distribution is notably higher than that of other methods owing to the considerable volume which is analysed. Therefore OES-PDA is mainly applicable for defects on the material surface. As a result of the spark dispersion, the exact

position of an inclusion is difficult to define. The position can be detected with an accuracy of $\pm 3\ mm$ [36].

4.3.1 Measuring Principle and Application

OES-PDA is based on the principle of Optical Emission Spectrometry. The sample is evaporated through a spark discharge. Subsequently the analysing elements are activated to optical emission and simultaneously ionised. The energy is transferred through a high frequency field in which free electrons are accelerated. Due to the collision of the same with the atom body, the plasma is heated. The emitted photons, which exhibit a characteristic wavelength of a the specific element, are detected by a spectrometer. Moreover the measured intensity is proportional to the concentration of the element in the sample.

OES is traditionally used for process control in steel works. The electronic setting has been modified for OES-PDA to enable acquisition of pulse intensities after each single spark. Thereby simultaneous spectra are obtained for the various elements present in the inclusions. The basic principle is that an electric discharge hits an inclusion in the steel sample which causes a signal peak. The intensity levels between inclusions and matrix differ: the highest intensity pulse represents on inclusion, while the lowest is attributed to dissolved elements in the matrix. This context is illustrated in **Fig. 4-3** [36, 37].

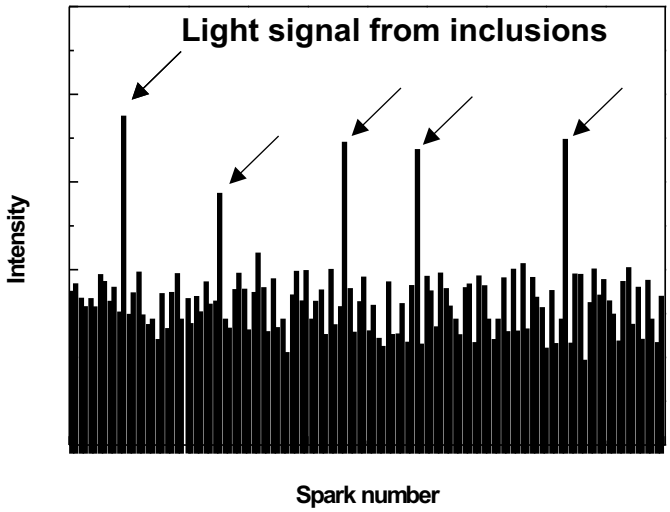

Figure 4-3: *Intensity contrast between inclusion and matrix for OES-PDA [36].*

Size distribution and chemical composition of inclusions can be determined by evaluating each single spark, while the matrix can be analysed by observing of a longer period. The sample preparation is very straightforward, involving only a grinding of the surface for an optimal sparking [37]. Generally, OES-PDA is essentially applied for rapid secondary metallurgy analyses. Therefore the inclusion content can be analysed directly during the ladle treatment. Furthermore this method opens an alternative to conventional practices of oxygen measurements [38].

4.4 Computer Tomography

The computer tomography (CT), is a method often used in medical diagnostics. Cross sections of an analysed object are detected and digitally evaluated. Thereby 3-dimensional perspectives can be created through several superposed tomograms.

4.4.1 Basic Principle

Firstly, X-rays are emitted from an X-ray tube and impinge on the sample, thus attenuating the beam intensity. As a result of the rising intensity contrast, conclusions concerning the inside of the sample can be drawn by comparing emitted and measured radiation.

Owing to the constantly rising requirements on material testing as well as increasing component complexity, the conventional computer tomography was enhanced. In order to avoid the superposing of single layers for obtaining a 3-dimensional perspective, the so called cone beam tomography was developed [39]:

4.4.2 Cone Beam Computer Tomography

In contrast to the formerly used method, the cone beam computer tomography (CBCT) directly permits the detection of 3-dimensional images via a rotation of the analysed object by 360°. During this rotation hundreds of 2-dimensional projections are recorded, out of which a 3-dimensional image is reconstructed applying mathematical algorithms.

It is evident that the resolution is equal for all directions in space. Using CBCT inclusions, inhomogeneities, blowholes and density variations can be detected with respect to their location and geometry in the whole volume.

The application of CT and CBCT is limited by the maximum possible object dimensions and radiographic length. Usually sizes between $3 - 600\ mm$ with a spacial resolution of app. $3\ \mu m$ are realistic. Analysing parts with large wall thicknesses frequently results in lacking penetrability and can cause misinterpretations. A major drawback of every CT is that chemical compositions of an inclusion cannot be defined [40]. CBCT is however a multifunctional method in the field of non-destructive material testing. It is generally used for quality checks as well as random inspections.

4.5 Electron Probe Micro Analysis

The currently most exact method of non-destructive testing available is Electron Probe Micro Analysis (EPMA). With this mehod, the detection limit lies in the region of parts per million.

4.5.1 Measuring Principle

The basic principle was developed in the 1950's by Castaing [41]. He suggested an analysing method that is based on the comparison of two radiation intensities with the same wavelength – the characteristic radiation of the same element in the sample and in a standard. The schematic configuration of the Castaing EPMA is shown in **Fig. 4-4**. Principally an electron beam is generated by an electron source. Bundled through a two lens optical system it reaches the sample with a diameter of about $1\ \mu m$. The thereby activated X-rays are analysed by a so-called WDX (Wavelength Dispersive X-ray)-detector and the intensity of the relevant line is measured. Through comparison with a standard, the chemical composition of the sample can be evaluated [41].

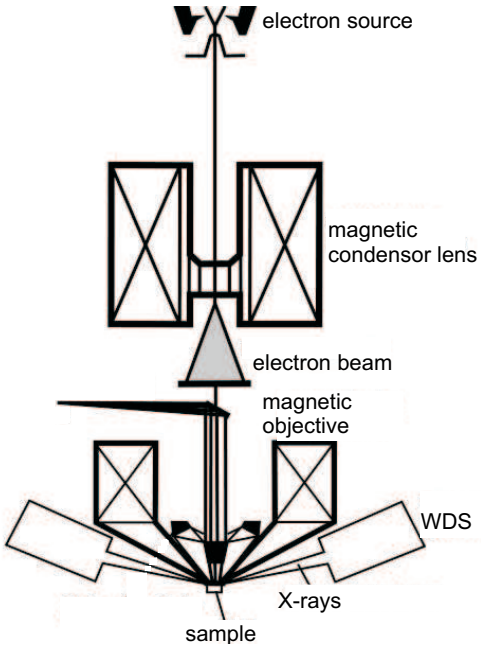

Figure 4-4: *Schematic configuration of the Castaing EPMA [41].*

A further development of the Castaing EPMA was achieved by Wohlleben *et al.* [42]. Here, the electron beam is deflected electromagnetically. The heavier the element, the more electrons are reflected. A high impulse rate – meaning a high concentration – results in a high intensity on the radiograph. In this way, EPMA can be used for characterising non-metallic inclusions. In the past 40 years the EPMA has been constantly improved, nowadays enabling a chemical and analytical identification of microscopically small inclusions, as well as inhomogeneities and phases [43].

4.5.2. The WDX System

Principally, detection systems are either based on WDX or EDX (Energy Dispersive X-rays). Both methods can be used with an EPMA, although modern equipments are mainly coupled with WDX systems, wherefore this type is described in detail. Specified information on the EDX method is given in section 4.6.

The function of WDX detectors is the separation of characteristic lines of different elements. The main component of this spectrometer type is the analysing crystal with specific

lattice spacing that is used to diffract the characteristic X-rays on their way from the sample into the detector. According to Bragg's law, the position of the crystal determines which wavelength of the X-rays is analysed. Thus only X-rays from one specific element can be measured at a time [43].

Two types of crystals which are illustrated in **Fig. 4-5** are in use today – the so-called Johann geometry and the geometry after Johansson. In the first case, the diffracting crystal is bent to a radius of $2 \cdot R$, where R is the radius of the focusing circle, called the Rowland circle. The second more precise type has the crystal bent to a radius of $2 \cdot R$ which is hence ground to a radius of R, so that all of the points of reflection lie on the Rowland circle. Consequently all of the X-rays originating from the point source on the sample are diffracted over a greater percentage of the crystal surface and are focused at the same point on the detector, thus maximizing the collection efficiency of the spectrometer [44].

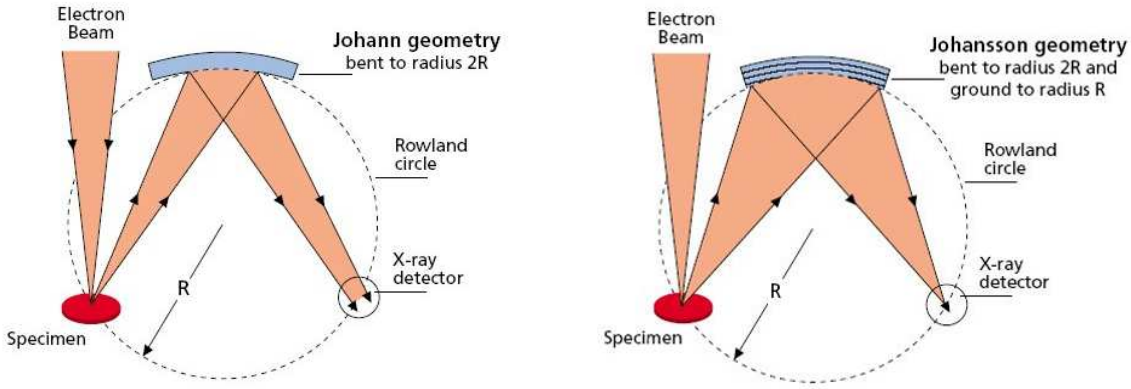

a) b)

Figure 4-5: *Crystal types of WDX systems: a) Johann-Geometry and b) Johansson-Geometry [44].*

Today most EPMA systems work with several spectrometers at different geometric positions. Crystal type and number are variable, whereby usually 3–4 crystals are used. While multi-layer crystals are used for the detection of light elements (Be-F), LiF-crystals are applied for detecting elements with higher atomic numbers [43].

4.5.3 Accuracy of Analysis

According to today's state of the art, all elements between Beryllium (atomic number 4) and Uranium (atomic number 92) can be detected by the EPMA. Like with every other analysing method some possible sources of failure exist. One of them is an exceedingly high Bremsstrahlung, since the ratio of measurement signal to underground noise is decisive for element verification. A second problem are optimal excitation conditions which are always a compromise between optimal excitation and preferably low absorption. Moreover, line overlapping, especially when detecting light elements, and matrix effects can possibly provoke errors, because a clear element identification is hindered. In addition adsorption, especially affecting light elements, and fluorescence, which appears if the primary radiation of an element activates a lighter element, have to be considered in some cases.

4.6 Scanning Electron Microscopy

The SEM in combination with an EDX is one of the most frequently used method for micro inclusion characterisation. In contrast to a conventional optical microscope, it provides not only morphological data, but gives also information on the chemical composition of inclusions. Furthermore it provides a remarkable sharpness and resolution and is characterised by a very large magnification interval between app. $10\times$ and $100,000\times$. The SEM provides information on size, composition and distribution of nonmetallic inclusions. Concerning the inclusion analysis the same aspects as described for the EPMA should be considered. Lastly, matrix corrections as described in 7.1.2 are inevitable, because generally X-rays are not only emitted by inclusions but also by the surrounding steel matrix.

4.6.1 The Device

An electron beam, generated by an electron gun, is attracted towards the anode through a condenser lens which bundles the beam. Subsequently the beam is focused on the sample surface through the objective as a very small dot. Inside the objective several deflectors which

are supplied by a changeable voltage are situated. Thereby generating a magnetic field, the deflected beam is conducted in a controlled matrix form. **Fig. 4-6** shows a schematic layout of a scanning electron microscope. A series of complex interactions occur when the electron beam impinges on the sample: Secondary electrons (SE) and back scattered electrons (BSE) are stroken out and are collected in front of the detector, transformed into a voltage peak and amplified [45]. The main components of a SEM are therefore:

- Electron beam generating system,
- Lens system,
- Detectors for registration of generated secondary signals,
- Signal converting, influencing amplifiers and display.

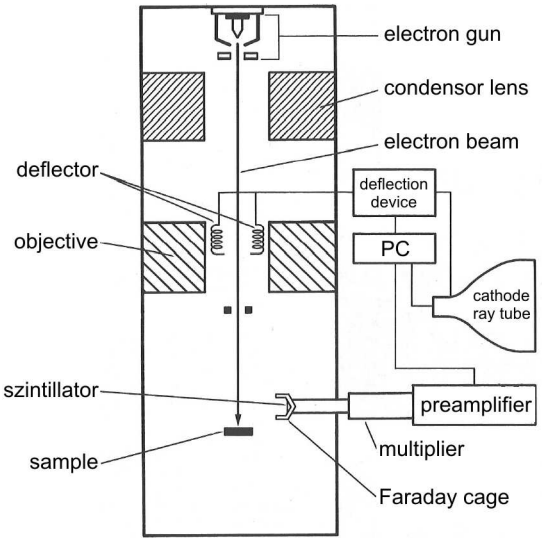

Figure 4-6: *Schematic layout of a Scanning Electron Microscope [45].*

4.6.2 Electron Beam-Sample Interactions

Once the accelerated electrons – primary electrons (PE) – impinge on the sample, there are two possibilities of back scattering: Elastic scattering takes place once the PE are diverted by positive charged atoms and electrons wherefore they change their directions but do not

loose energy – these electrons are called back scattered electrons (BSE). Inelastic scattering however arises, if PE render part of their energy through interactions with shell atoms – so-called secondary electrons (SE) are generated. The standard image of a SEM is based on secondary electrons. Interactions between primary electrons and the atomic nucleus lead to the so-called Bremsstrahlung. Cathode luminescence occurs, if SE recombine with "holes" which can emerge through electron irradiation in certain metals and therefore lead to an emission of photons with wave lengths in the visible and infrared region. Characteristic X-rays are a result of ionisation of the inner shells. Beside X-rays, Auger electrons are by-products of the ionisation through PE. The energy of these electrons is typical for the chemical composition of the first atom layers under the sample surface. These signals can provide information not only about the surface appearance or topography of the sample but also about its composition and microstructure. A schematic illustration of these electron transitions is given in **Fig. 4-7**.

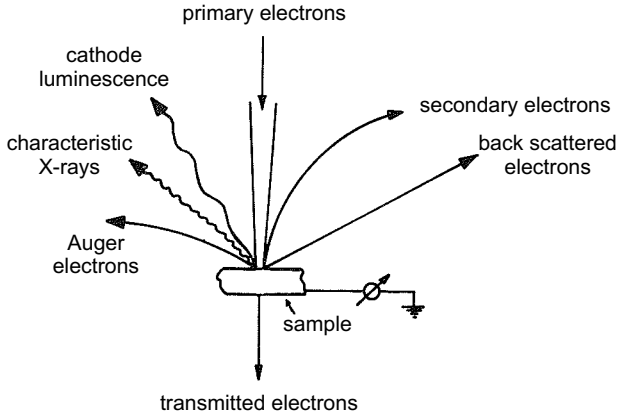

Figure 4-7: *Electron interactions in a Scanning Electron Microscope [43].*

All these interactions are scattering processes, where the degree of scattering is not exactly limited. For a better understanding the remaining energy of incident electrons as well as the area, where interaction take place are restricted. Consequently only the drop shaped area in which interactions take place most probably is described, as illustrated in **Fig. 4-8**. For compact samples the interaction volume (depth and width) changes directly with accelerating voltage and contrariwise with atomic number of atoms. The atomic number of

the searched point highly influences the contrast in BSE mode. Generally, points of high atomic number are shown brightly, points of low atomic number are displayed darkly. Usual nonmetallic inclusions have much lower atomic numbers than the steel matrix. Out of this reason inclusion characterisation is possible with SEM/EDX [43, 45].

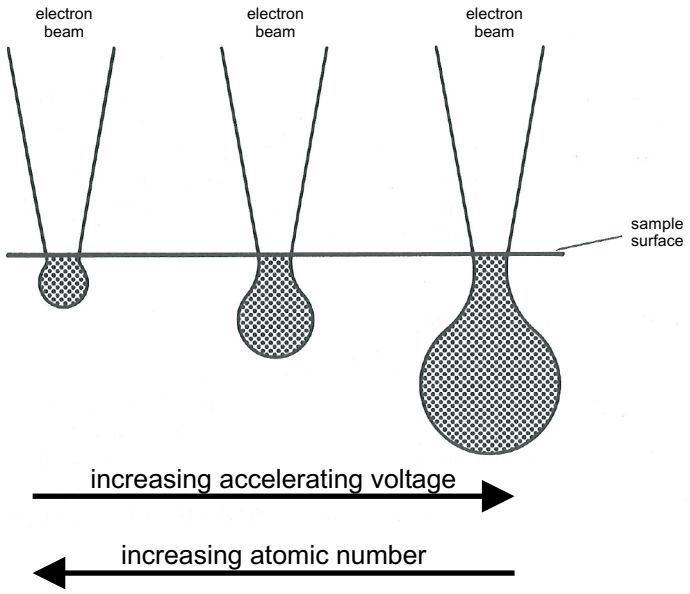

Figure 4-8: *Dependency of interaction volume on accelerating voltage and atomic number [45].*

4.6.3 EDX System

Contrary to the beforehand illustrated WDX spectrometer type, EDX systems are based on energy dispersion. With this type, all backscattered electrons – independent of their wavelength – hit a Silicon semi-conductor detector cooled by liquid nitrogen. **Fig. 4-9** shows a schematic circuit diagram of an EDX detector [46].

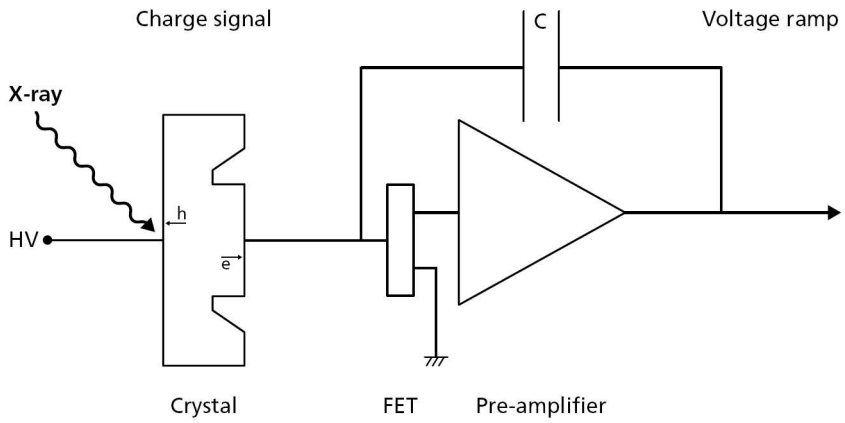

Figure 4-9: *Schematic circuit diagramm of an EDX detector [46].*

The energy of each individual X-ray is converted into a voltage signal of proportional size. The components of an EDX detector and their respective functions are [46]:

Collimator assembly: Provides a limiting aperture through which X-rays must pass to reach the detector. This ensures that strayed X-rays are not included in the analysis.

Electron trap: Pair of permanent magnets that strongly deflect any passing electrons in order to avoid background artefacts.

Window: Provides a barrier to maintain a vacuum within the detector whilst being as transparent as possible to low energy X-rays.

Crystal: Semiconductor device that converts X-rays of a particular energy into electric charge of proportional size.

Field effect transistor (FET): First stage of the amplification process that measures the charge released in the crystal by an incident X-ray and converts it to a voltage output.

Cryostat: The electronic noise of the detector has to be minimised by cooling the crystal and the FET.

4.6.4 Comparison EDX-WDX

Generally, EDX provides several advantages in comparison to WDX. The overall costs of a WDX system are approximately four times higher than for a EDX system. The essen-

tial advantage of EDX lies in the analysing time: Whilst an EDX system can detect the whole spectrum simultaneously, WDX can only detect one element per detector at a time. Therefore a complete analysis of all elements of the periodic table requires a few minutes with an EDX and several hours with a WDX. Nonetheless, EDX systems also have some limitations: Compared to WDX its spectral resolution – the ability of separating two lines of adjacent elements correctly – is lower. This feature is particulary important regarding light elements, since the K_α lines of B, C, N, O and F often overlap in the lowest, still detectable region [43, 45]. A comparison of WDX and EDX characteristics is shown in **Tab. 4-1** [46].

Table 4-1: *Comparison of WDX and EDX characteristics [46].*

Characteristic	WDX	EDX
Efficiency of X-ray collection	Low – typical solid angle around 0.001 steradians*	Higher – typically $0.005-0.1$ steradians
Beam current	High – typically minimum of 10^{-8} A because of low collection efficiency	Low – beam currents can be as low as 10^{-10} A
Resolution	Good – depends on crystal, but typically of the order of $5-10$ eV	Energy dependent – typically < 133 eV measured at Mn (K_α 5.9 keV)
Limit of detection	< 0.01 %. Depending on matrix and element can be as low as parts per million	Typically $0.1 - 0.5\%$
Speed of analysis	Slow – only one element can be analyzed at any one time by one crystal – Serial detection	Fast – all elements are effectively analysed simultaneously – Parallel detection
Quantitative analysis	Easy – measure peak minus background	Complex – algorithms needed for peak deconvolution and background subtraction

* Steradian is defined as the solid angle subtended at the center of a sphere of unit radius by a unit area on the surface of the sphere. There are $4p$ steradians in a sphere. Steradians are dimensionless.

4.7 Methods Comparison

In the previous sections several methods for the characterisation of nonmetallic inclusions have been described. Depending on the employed method, different analyses are provided – the spectrum reaches from the simple detection of the existence of nonmetallic inclusions to a concrete description of size, composition and distribution. A general prediction of the representativeness, accuracy and potentials of a certain method is rather difficult, owing to the large amount of influencing factors.

In **Tab. 4-2** the methods are compared in their advantages and disadvantages when using them for inclusion characterisation. It is apparent that no general evaluation can be proposed. The listed detectable inclusion sizes are taken from several publications [26, 43, 35] dealing with inclusion characterisation and shall provide an informative basis for the respective size dimension. Certainly these values vary in a certain range.

Table 4-2: *Comparison of methods.*

	Chart comparison	OES-PDA	CBCT	EPMA	SEM
morphological data	✘	✘	✔	✔	✔
size distribution	✘	$\sim$	✔	✔	✔
chemical composition	✘	✔	✘	✔	✔
detectable inclusion size	$2-12\ \mu m$	$>30-40\ \mu m$	$2-12\ \mu m$	$>1\ \mu m$	$>1\ \mu m$
analysed sample volume	moderate	small	large	small	small
sample preparation	extensive	facile	facile	extensive	extensive
analysing time	app. $1\ h$	$<10\ min$	$1-5\ h$	$1-5\ h$	$1-5\ h$

5 Automated SEM/EDX Cleanliness Analysis

In the present thesis the cleanliness of steel is investigated by an automated SEM/EDX analysis. Two different types of analysing equipments are used: Firstly, the Personal Scanning Electron Microscope (P-SEM) installed at voestalpine Stahl GmbH in Linz and secondly the INCA system arranged at the Chair of Metallurgy at the University of Leoben. Both systems make it possible to determine chemical composition, size, shape and position of a large amount of nonmetallic inclusions automatically. In this chapter the fundamentals of both methods together with their similarities and differences are discussed.

5.1 Differences to Manual Methods

As described in chapter 4, manual SEM/EDX is a common combination for inclusion characterisation. However, there are limitations to the manual analysis:

- Analysing a few characteristic inclusions may not represent the whole sample, even for a relatively homogenous sample,
- Finding a single inclusion in the presence of thousands can be difficult or even impossible,
- Obtaining enough individual inclusions to produce statistically significant information by manual analysis is very time consuming.

Furthermore it is generally impossible to analyse nonmetallic inclusions of all size classes simultaneously. As described in the last chapter, many methods for inclusion characterisation exist and each one is able to detect particles in a certain size range. A possible classification for the spectrum of methods and their average size distribution is given in **Fig. 5-1**.

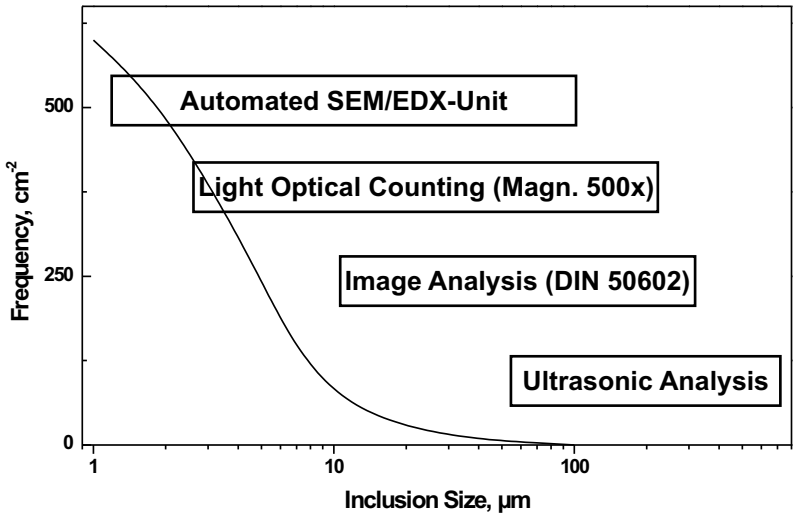

Figure 5-1: *Spectrum of methods for cleanliness analysis [47].*

It can be seen that automated SEM/EDX analysis features two essential advantages compared to other methods: The range of size detection capability as well as the number of detectable inclusions are larger than at other methods. Furthermore the possibility of rapidly relocating any particle for post-processing and additional data collection offers an essential advantage [47, 48].

5.2 SEM/EDX Conditions

The basis is a conventional Scanning Electron Microscope with secondary electron and backscattered electron detectors working under vacuum for both analytic methods. By the use of an EDX system elemental information of each analysed particle is determined. Nonmetallic inclusions are detected due to material contrast differences in the BSE image. Backscattered electron images are generally used in preference to secondary electron (SE) images as the contrast in BSE images is strongly dependent on the atomic number of the material which helps to differentiate between various phases. According to their grey scale value, inclusions are distinguished from the steel matrix using a threshold criterion based on the pixel intensity. Data on size, area and shape of each inclusion is calculated by a mathematic algorithm. Subsequently the EDX analysis determines the chemical composition of the particles. As a result a complete data set for each nonmetallic inclusion, including

parameters for position, size, length/width, as well as the chemical composition normalised in percent by mass is obtained. In both cases the scanned area is 100 mm^2 which is divided into approximately 400 measuring fields and scanned one after another. The measurement time varies between one and several hours depending on inclusion content of the analysed sample [47, 48]. **Tab. 5-1** shows the SEM/EDX conditions used for inclusion analysis in both methods.

Table 5-1: *SEM/EDX conditions used for inclusion analysis [47].*

Condition	P-SEM	INCA
Beam energy	15 kV	15 kV
Emission current	$30 - 35$ μA	100 μA
Vacuum pressure	8×10^{-4} Pa	9.45×10^{-4} Pa
Working distance	$18 - 20$ mm	15 mm
Detector mode	BSE	BSE
Magnification	600×	600×
Resolution	2048×1920	1024×960
Detectable inclusion size	$1 - 130$ μm	$0.7 - 100$ μm
Evaluation time for one particle	3 s	2.5 s

Both methods assign the detected inclusions into defined classes. A matrix correction is not executed. This is one of the reasons why P-SEM as well as INCA are coupled with an especially developed offline evaluation system, which is exactly adjusted on the analysed steel grades [47].

5.2.1 P-SEM

The automated SEM/EDX system is compounded by ASPEX and was installed at voestalpine Stahl Linz in 2002. The large sample chamber is equipped with a self-designed sample holder which allows manual loading of six samples. The samples are held at a standardised working distance of 20 mm. If required, information from a small digital camera set on the

sample chamber allows easy orientation and macronavigation on the sample surface. The quantification of EDX results is based on certified standards [47, 48].

5.2.2 INCA

The analysing time of this system is generally a little longer than for the P-SEM, although the EDX-analysis duration for evaluated particles is shorter. This is due to the fact that the P-SEM records the present SEM image, however not storing it. In contrast to the P-SEM, the INCA directly measures O, C and N with EDX analysis. As a consequence, the basis for inclusion classification is completely different. Detailed information concerning the test procedure are given in chapter 6.

5.3 Offline Evaluation System

Both systems are coupled with an offline evaluation method for handling the large amount of raw data and for defined classification as well as matrix corrections. The basic configuration is the same for both methods. The significant difference lies in the inclusion classes, which are described in detail below. A matrix correction, which is inevitable for correct inclusion classification, is done in both cases, because a number of factors influence the number of X-rays generated at any point on the sample. Next to the extent of absorption within the sample, the fraction of the incident electron beam that is not backscattered as well as the contribution to the signal from X-ray fluorescence as the X-rays traverse the sample, are decisive causes for the necessity of the matrix correction.

5.3.1 Inclusion Classes

As already mentioned the detected particles are categorised in an inclusion cluster in order to obtain detailed and representative information on type, size and distribution of inclusions. The systematic for P-SEM classification is discussed in the next section. As far as INCA classes are concerned, details are given in chapter 7.

5.3.1.1 P-SEM Inclusion Classes

In the offline evaluation of the P-SEM results, a specially designed algorithm categorises the detected particles into 23 inclusion classes. Since O, C and N are not analysed with the EDX in this case, the contents of these elements must be estimated through the contents of the other inclusion forming elements. Since this evaluation system was specially developed for steel grades produced at voestalpine Stahl GmbH, it is apparent that the defined inclusion classes do not completely match for steels produced at Böhler Edelstahl GmbH. Moreover the exact compositions and the underlying algorithm are not published by Nuspl *et al.* [47]. The inclusion classes as well as their explanation are shown in **Tab. 5-2**.

In order to establish an INCA inclusion cluster for PH 13-8 Mo with a systematic similar to that of P-SEM, several SEM/EDX analyses – automated as well as conventional – are necessary. The next chapters describe the INCA test procedure and the evaluation process.

Table 5-2: *Listing of P-SEM inclusion classes [47].*

Class	Inclusion type	Description
1	Al_2O_3	Alumina inclusion
2	CA	Calcium aluminate
3	CA-CaS	Calcium aluminate with calcium sulfide
4	CA-(Ca, Mn)	Calcium aluminate with calcium, manganese sulfide
5	$MgO{\cdot}Al_2O_3$	Magnesium spinel
6	$MnO{\cdot}Al_2O_3$	Manganese spinel (galaxite)
7	Mn-Silicate	Manganese silicate
8	Al-Silicate	Aluminium silicate
9	Mn-Al-Silicate	Manganese-aluminium silicate
10	CaO-CaS	Calcium oxide or calcium oxide with calcium sulfide
11	(Mn, Fe)S	Manganese-iron sulfide
12	TiS	Titanium sulfide
13	(Mn, Fe, Ti)S	Manganese-iron-calcium-titanium sulfide
14	CaS	Calcium sulfide
15	(Mn, Fe, Ca, Ti, Mg)S	Manganese-iron-calcium-titanium-magnesium sulfide
16	OS	endogenous oxide with sulfide
17	OCN	Oxi-carbo nitride
18	OCN-S	Oxi-carbo nitride with sulfide
19	CN	Carbo-nitride
20	CN-S	Carbo-nitride with sulfide
21	Exogenous+Na	Exogenous inclusion with sodium content
22	Exogenous	Exogenous inclusion
23	Unid	Particle not categorised

6 Experimental Procedure

6.1 Sampling

Several samples taken during the production of the steel grade PH 13-8 Mo at Böhler Edelstahl GmbH were analysed on their inclusion content. **Tab. 6-1** shows the labelling of all analysed samples including a short description, dimensions and other notes. While samples A–D are taken from different melts for preliminary tests, samples E–H were taken from the same melt at different process steps. This allows an exact tracing of inclusion development and modification during the whole production flow.

Table 6-1: *Analysed PH 13-8 Mo samples.*

Sample	Origin	Notes
A	rolled material	longitudinal sample position
B	rolled material	transversal sample position
C	VIDP sample	sample out of the melt, forged
D	residual melt after ingot casting	forged
E	VIDP sample	forged, located 1/4 above floor
F	residual melt after ingot casting	forged, center location
G	rest electrode of VAR	forged as bar material
H	rolled material	longitudinal sample position

The specific sample origins in the production flow are shown in **Fig. 6-1**. **Figs 6-2** and **6-3** illustrate the position in the rolled material, where samples A, B and H were taken.

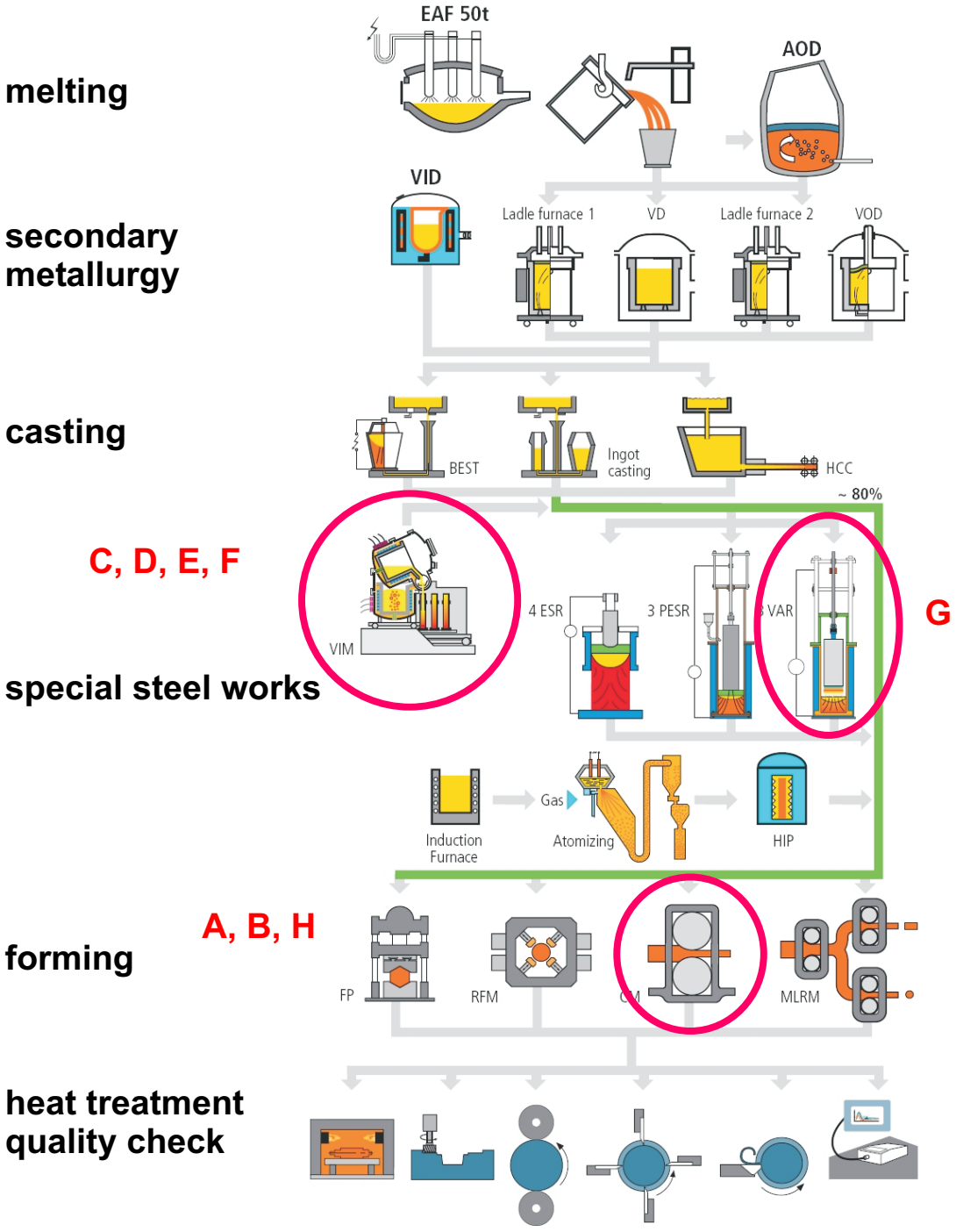

Figure 6-1: *Specific sample origins of PH 13-8 Mo at Böhler Edelstahl GmbH [50].*

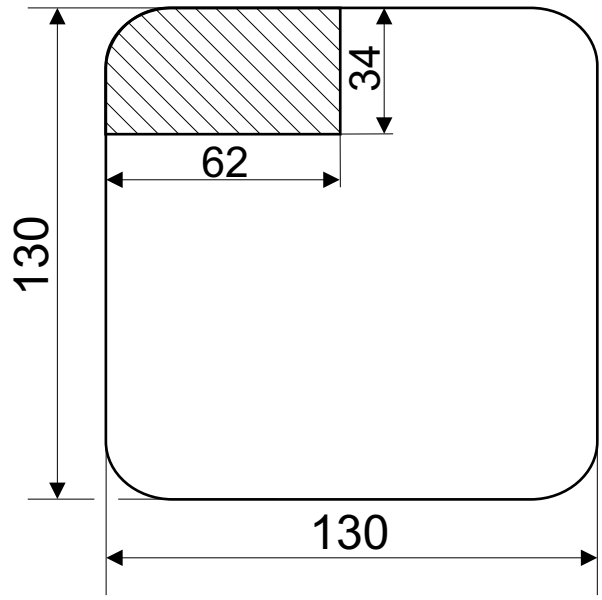

Figure 6-2: *Origin of samples A and B (shaded area) from the rolled material.*

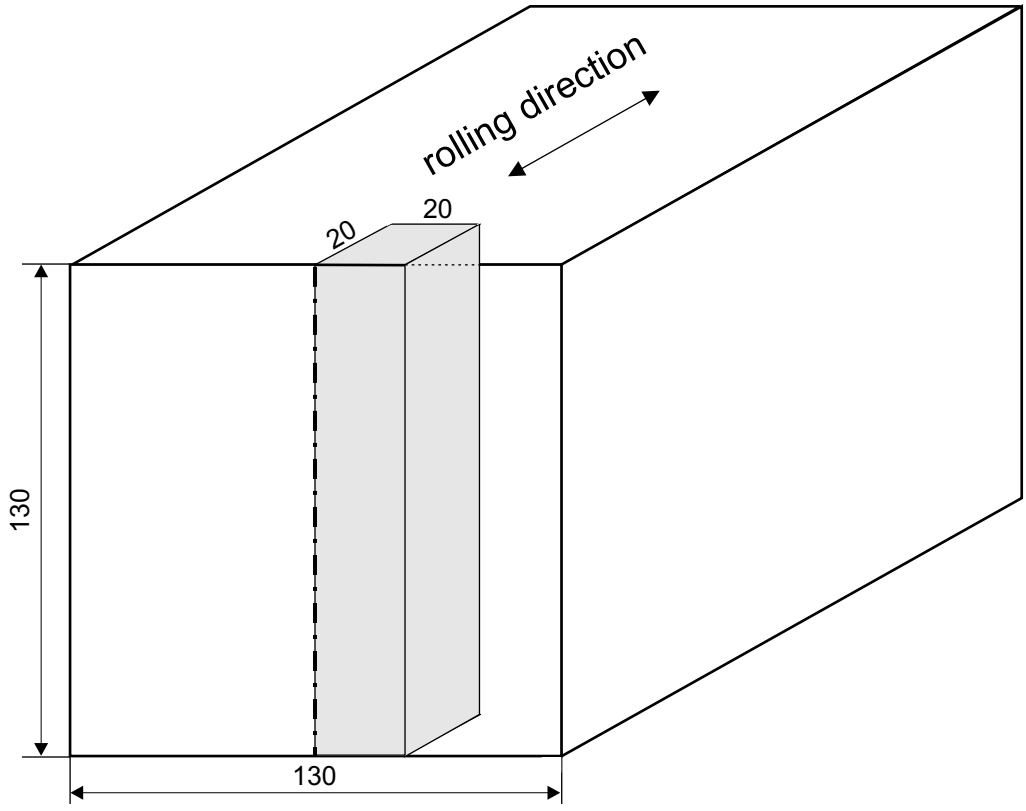

Figure 6-3: *Position of sample H.*

In addition to the mentioned samples of PH 13-8 Mo, one sample of the steel grade H11 (X38CrMoV5-1) is analysed in order to prove the transferability of the defined inclusion classes on another steel grade. The description of this sample is found in **Tab. 6-2**.

Table 6-2: *Analysed H11 sample.*

Sample	Origin	Notes
I	rolled material	longitudinal sample position

All named samples are investigated with the INCA system at the Chair of Metallurgy. Samples A–D and I are also analysed with the P-SEM at voestalpine Stahl GmbH at Linz.

6.2 Sample Preparation

A metallographic preparation is necessary for a SEM/EDX inclusion characterisation. To avoid the break out of inclusions during sample preparation, every sample is only manipulated by hand. Moreover, every sample is embedded in order to facilitate preparation. The same sample preparation is used for both cases – P-SEM and INCA – thereby ensuring comparability. Depending on the original sample size the final sample surface lies between $12 \times 12\ mm^2$ and $25 \times 25\ mm^2$, whereof $10 \times 10\ mm^2$ are analysed.

The metallographic preparation includes wet grinding at four different grainings (180, 320, 800 and 1200) and polishing the sample with a medium hard (3 μm) as well as a soft (1 μm) cloth. The samples should be analysed shortly after preparation in order to prevent a scratching of the surface by dust particles. Moreover, an absolutely planar surface of the sample is essential for a constant matrix grey scale value. A variation in matrix grey scale value would cause problems for automated analysis.

6.3 Experimental Setup

The two main components of experimental setup are the Scanning Electron Microscope and the EDX System. The SEM installed at the Chair of Metallurgy is a Quanta 200 3D from the company FEI consisting of the column (wolfram cathode with automated filament saturation) and the sample chamber. As also illustrated in **Fig. 6-4**, the EDX system consists of three basic components:

- X-ray Detector,
- Pulse Processor,
- Analyser.

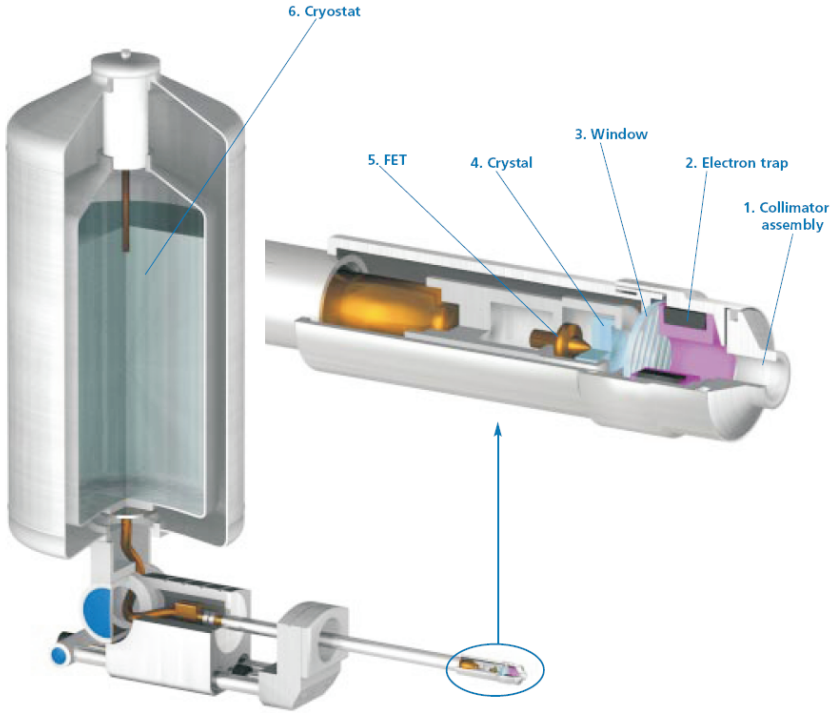

Figure 6-4: *Schematic construction of the used EDX detector [46].*

To determine the energy of each detected X-ray, the electronic signal is measured by the pulse processor. As a last step the analyzer displays the X-ray data.

6.4 Test Procedure

In this section the automated INCA test procedure is described. Firstly, the definition of several settings, shown in the chart in **Fig. 6-5**, is required. They are explained in the following.

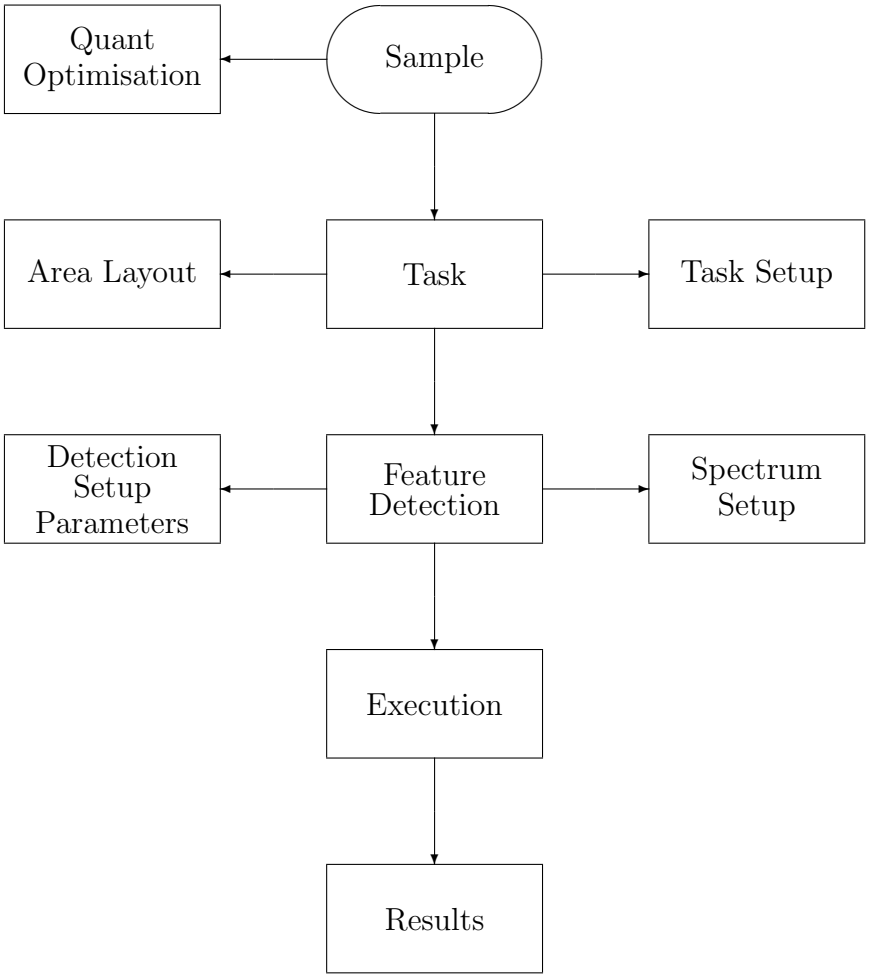

Figure 6-5: *Programme flow.*

6.4.1 Quant Optimisation

Basically, the quant optimisation controls the stability of the beam current. The number of counts in the elemental peak from a known standard is the basis for conducting a quant optimisation: By measuring the position of this peak, the system is finely tuned for acquiring a high quality spectrum. Presently, a copper strip fixed at one edge of the sample surface is

used for performing the quant optimisation. Generally, at least one optimisation should be conducted before every measurement in order to get reliable results.

6.4.2 Task

All parameters which define the detection, data acquisition, measurement and classification of features, meaning an inclusion, are stored. A database, on which the subsequent feature analysis should be based, has to be chosen.

6.4.2.1 Area Layout

Here the area over which the feature scan is done, is defined by specifying two stage positions (opposed vertices of a rectangle) on the sample surface. In the present analyses the area of the rectangle is always 1 cm^2, schematically shown in **Fig. 6-6**. The defined areas is hence devided into app. 400 measuring fields, provided that a resolution of 1024×960 is used. For different resolutions the number of measuring fields is changed accordingly.

In addition to defining the analysing sample surface, two reference fields on the sample must be set. The first is the copper reference for the quant optimisation given through the tapped copper strip. The second is an iron reference field containing some significant feature for following calibration.

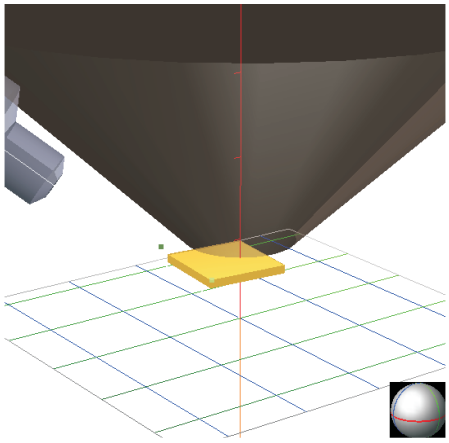

Figure 6-6: *Schematic illustration of an area layout.*

6.4.2.2 Task Setup

In this category, some termination criteria of a measurement can be defined thus avoiding the collection of excessively large amounts of data and reducing the time spent for analysing samples. Different types of termination limits can be set:

- Termination of number of features in a field,
- Termination of total number of features in the area,
- Termination of total number of features in a sample (if several areas are analysed).

If one of the set limits is reached, the analysis of the current field, area or sample is stopped and the programm automatically moves onto the next field, area or sample. For the present analyses a maximum number of $20,000$ features in the analysed area was defined, although the limit was never reached in any of the analyses.

6.4.3 Feature Detection

Here the feature detection is optimised through two steps:

- Calibration against a standard,
- Setting of thresholds.

6.4.3.1 Calibration

The backscattered electron detector signal is used to set the upper and lower grey level thresholds. It is important to get these upper and lower threshold settings correctly, since unwanted features may be detected otherwise. The chance of missing features arises at threshold settings higher than optimum. **Fig. 6-7** demonstrates the difference in grey tone between matrix and inclusions, which are characterised by a significantly darker grey scale value than the matrix.

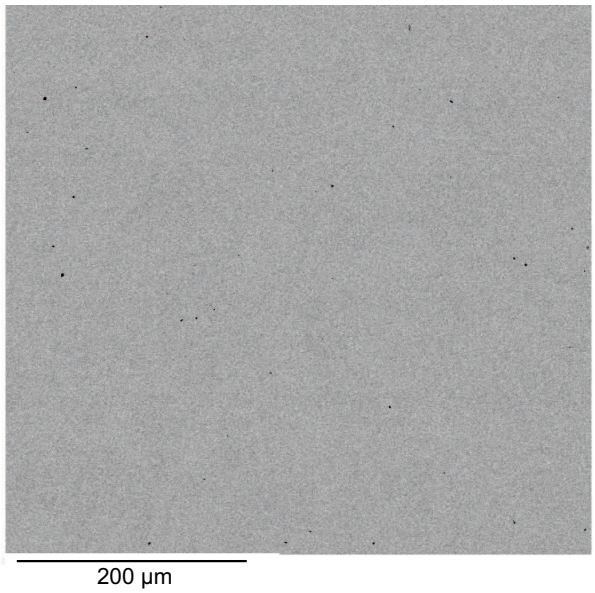

Figure 6-7: *Differences in grey scale value between inclusions and matrix.*

6.4.3.2 Threshold Setting

A diagram as given in **Fig. 6-8** shows the frequency distribution of the grey scale value, which represents the signal intensity. The minimum and maximum values for grey scale value can directly be determined.

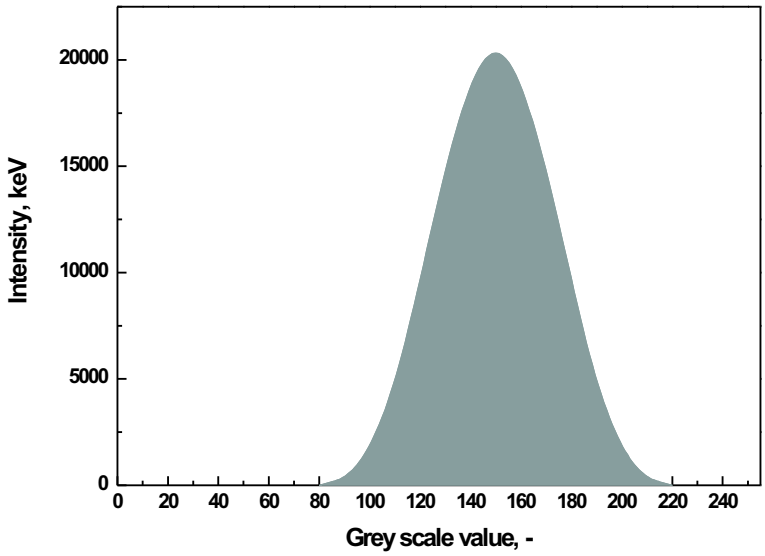

Figure 6-8: *Frequency distribution of grey scale value.*

The number of inclusions detected in one field is highly affected by the settings of grey scale value. Out of this reason an appropriate adjustment of contrast and brightness of the SEM image is inevitable, otherwise resulting in analytic errors. The threshold setting is certainly one of the most important factors influencing automated inclusion analysis.

6.4.4 Setup Parameters

A number of parameters can be set to optimise the feature detection performance. In the spectrum setup the number of EDX passes performed as well as the analysing time in seconds can be selected. All measurements in this thesis are carried out with one EDX pass and an analysing time of 2.5 s.

6.4.4.1 Resolution and Magnification

A higher resolution will allow a lower magnification to be used for the same pixel size. This will reduce the time taken for acquisition over an area because fewer stage movements are required.

The area scanned for each field increases with a reduction of magnification, resulting in the analysis of a fewer number of fields for covering the same area. Although the overall speed of the analysis increases, because the number of fields is reduced, a too small magnification is not reasonable regarding desirable detecting inclusion sizes.

An important part within the present thesis is to determine the optimal combination of resolution and magnification regarding time of analysis and number of detected inclusions: Out of several analysis (see chapter 7) a magnification of $600\times$ and a resolution of 1024×960 has proven to be optimal.

6.4.4.2 Minimum Feature Area

In this section a minimum detected feature area has to be set. Features in the specified area smaller than the defined value in pixel (abbreviated as px) are hence ignored during the analysis.

For this purpose, length and Equivalent Circle Diameter (ECD) in microns are calculated. The ECD of a feature area is defined as shown in Eq. (6-1):

$$\mathrm{ECD} = \sqrt{\frac{4 \cdot A}{\pi}} \tag{6-1}$$

A.....feature area

In order to find an appropriate setting several analyses with different values of minimum feature area are made. **Fig. 6-9** shows a comparison of size distributions obtained for a minimum feature size of 9 px and 3 px.

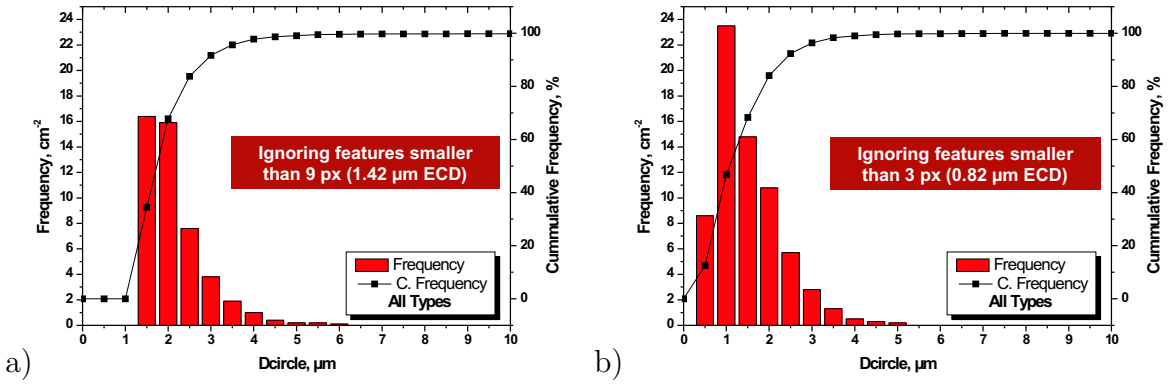

Figure 6-9: *a) Size distribution for a minimum feature size of 9 px and b) Size distribution for a minimum feature size of 3 px.*

In the present case, 3 px are chosen as a representative value, which leads to an average minimum inclusion size of about 0.8 μm ECD.

The double counting of features as a result of overlapping within two fields is prevented through the so-called guard zone. Any features which lie across the guard zone are included in the feature count, whilst those that are fully within the guard zone or touch the edge are excluded. Thereby each feature is only counted once. The guard zone is aligned to the right and lower edges of the field. Presently, the guard zones amounts to 15 px.

6.4.5 Execution and Results

During the test procedure the currently analysed SEM image as well as the complete schema of the area layout are displayed. As shown in **Fig. 6-10** inclusions detected in already

analysed fields are registered in the area layout. In this way the development of the inclusion distribution can be observed. Furthermore morphological and EDX spectra of the currently analysed feature combined with a summary of already detected particles are shown.

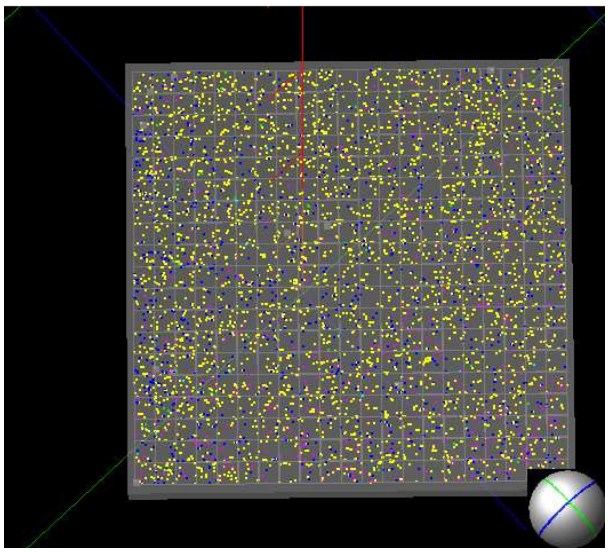

Figure 6-10: *Schema of an analysed area layout including already detected inclusions.*

As a result measurement details, the overall detected number of features and special information about each single feature – morphological and quantitative data – are received. **Tab. 6-3** summarises the exemplary morphological data of a feature, whereby the position of the detected inclusion is indicated by the X- and Y-coordinates of the beam.

Table 6-3: *Morphological data of a detected feature.*

Area	2.92 μm^2
X-beam	212.5 px
Y-beam	494.5 px
Width	1.48 μm
Length	3.12 μm
Perimeter	7.5 μm
ECD	193 μm

Fig. 6-11 shows the EDX spectrum, where the peak intensity is shown over the energy, for the same inclusion and **Tab. 6-4** shows the corresponding mass percentages. Regarding

the quantitative data, it is apparent that no matrix correction has been executed by the programme itself. Out of this reason and in order to allow an exact inclusion classification, all raw data are transferred to an offline evaluation system, which is especially adapted to the analysed steel grade.

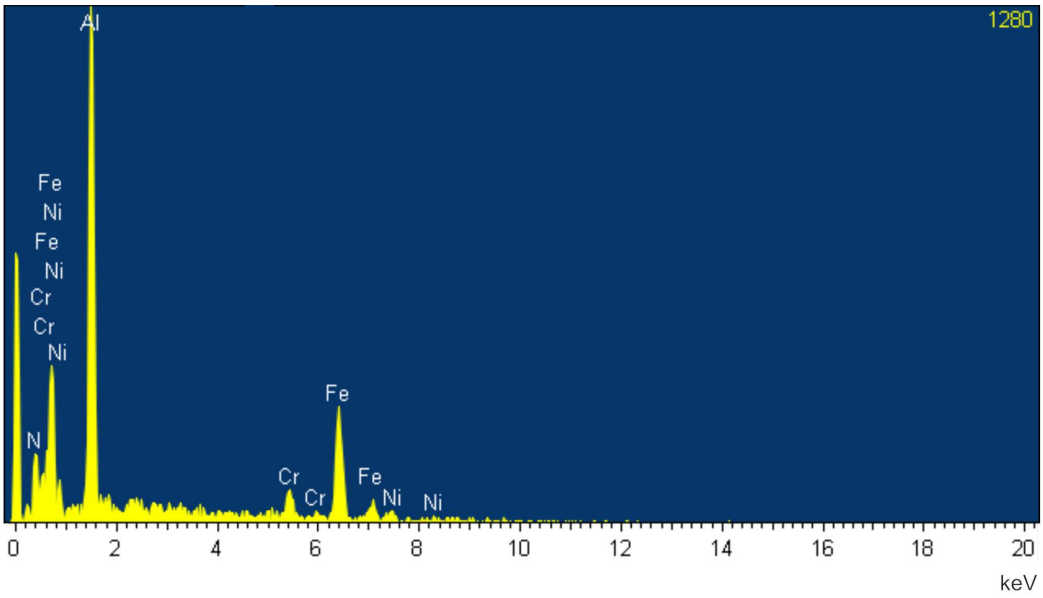

Figure 6-11: *EDX spectrum of a detected feature.*

Table 6-4: *Quantitative data of a detected feature.*

Fe	50.4 *wt.*-%
Ni	8.48 *wt.*-%
Al	22.3 *wt.*-%
N	11.92 *wt.*-%
Cr	6.9 *wt.*-%

7 Evaluation and Results

In this chapter first of all the process of software adaptation of the offline evaluation system for the PH 13-8 Mo is described. Furthermore the influencing parameters of the automated SEM/EDX analysis conditions on the amount and distribution of detected inclusions are analysed and an optimal adjustment is found in order to obtain representative results. The evaluation system is also tested on its applicability to other steel grades beside the PH 13-8 Mo and a comparison between P-SEM and INCA results shows the differences and difficulties for the inclusion characterisation owing to the large number of influencing factors. A detailed inclusion investigation of four samples of the same melt following the inclusion development and modification over the whole process completes the practical part of this thesis.

7.1 Software Adaptation

A special offline evaluation system for the inclusion characterisation is adapted for the analysed steel grade. All obtained raw data – meaning morphological and EDX results – are firstly transferred to the offline evaluation system. Thereafter a matrix correction is performed for all EDX data and the detected inclusions are categorised into different inclusion classes. One of the most important parts within this thesis is finding a reasonable classification cluster for the PH 13-8 Mo. Consequently the inclusion landscape of this steel has therefore to be analysed conventionally before using an automated method hence giving an impression of the possible inclusion types and thereof resulting limiting values of the different classes. Finally detailed information on inclusion type, size, frequency and distribution is obtained.

7.1.1 Inclusion Types

In order to get a first fundament for the classification cluster, samples A and B are conventionally analysed without using any automated method. The sample surface is scanned

for inclusions, which are easily distinguishable from the surrounding matrix in most cases because of their different grey scale values. Very small particles can only be identified with a very large magnification. The most frequently found inclusion types are AlN, Cr-Carbide, MA-Spinels and Al_2O_3. In the following some analysis results exemplary explained for an AlN – which is by far the most often found inclusion type – are illustrated.

Fig. 7-1 shows particles found on sample A and their corresponding EDX spectrum. Even though the matrix has not been corrected yet, it is apparent that these are AlN inclusions. **Fig. 7-2** illustrates the appropriate line spectrum of the detected AlN including the lines for Fe, Al and Cr.

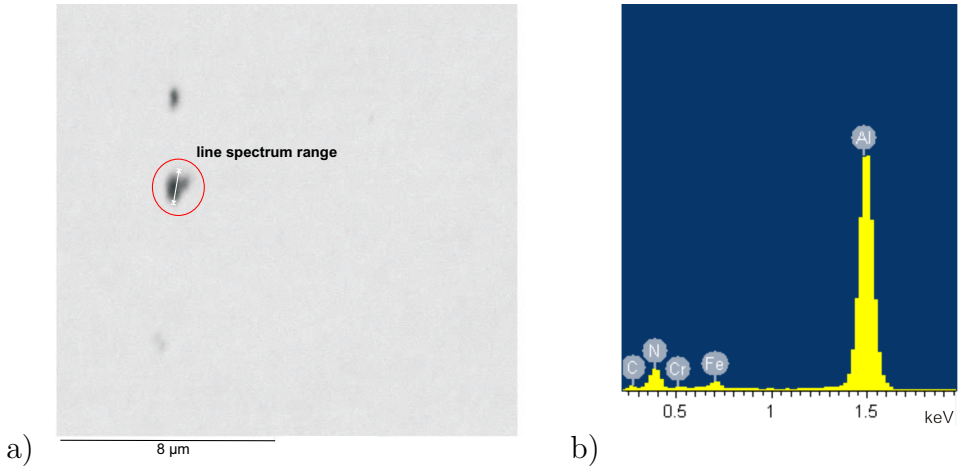

Figure 7-1: *a) SEM-image of detected AlN on sample A and b) Corresponding EDX spectrum.*

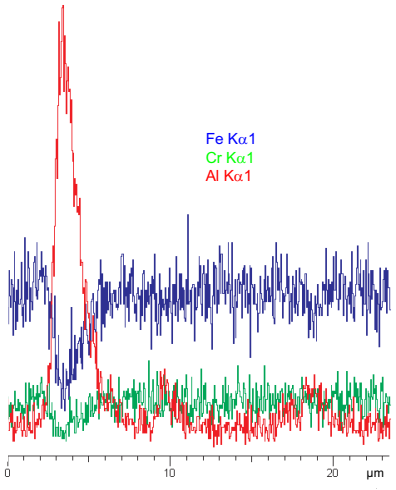

Figure 7-2: *Line spectrum of an AlN.*

It is shown that the inclusion itself is primarily depleted in Fe, while Al reaches its maximum in the inclusion center. The Cr content follows a comparatively constant distribution. AlN are also detected in a cellular arrangement in sample A as shown in **Fig. 7-3**. A comparison between the EDX spectra of the three marked particles is shown in **Fig. 7-4**. In all three cases the Al and the N peak are efficiently identifiable, which is an absolute must for getting representative results from an automated analysis.

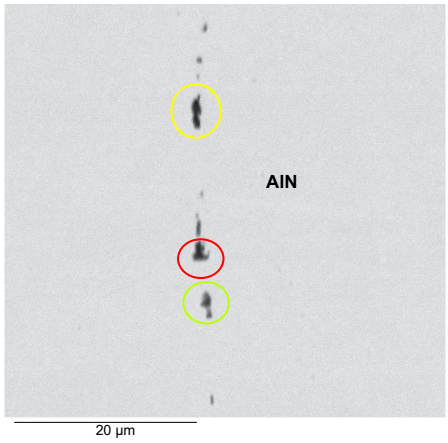

Figure 7-3: *Cellular arrangement of AlN in sample A.*

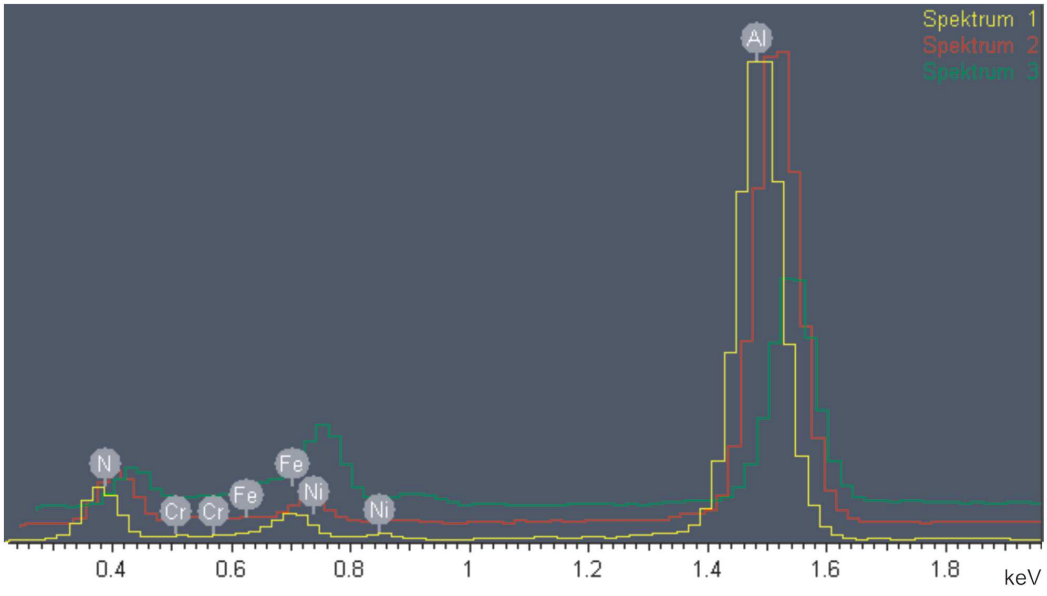

Figure 7-4: *Comparison of EDX spectra of three AlN particles.*

Evidently the inclusion types in sample B are similar to those of sample A, seeing that both were taken from the same block only distinguishing themselves in the sampling orientation. **Fig. 7-5** shows a Cr-Carbide inclusion found in sample B – a type which is also frequently detected.

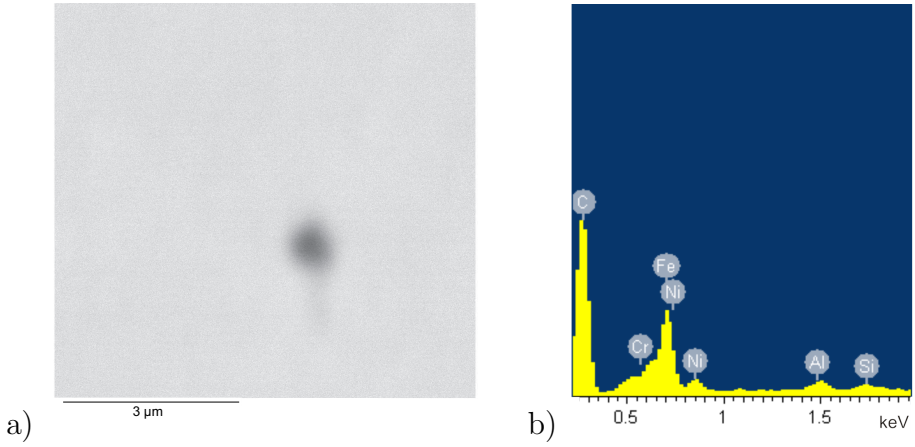

Figure 7-5: *a) SEM-image of detected Cr-Carbide on sample B and b) corresponding EDX spectrum.*

The displayed results provide a suitable basis for assembling an inclusion cluster, although no conclusion regarding the distribution of the inclusions over the sample can be drawn. The morphological appearance of detected inclusions is not studied in detail within this section, since a much better approach to topics such as size distribution is enabled by an automated analysis.

7.1.2 Matrix Correction

It has been mentioned that a matrix correction is vital for a correct and representative inclusion characterisation, since X-rays are generally not only emitted by inclusions themselves but also by the surrounding steel matrix. The detected iron content is especially affected by the particle size and increases with decreasing inclusion size. Assuming that inclusions do not contain iron – which is true for almost every inclusion type – the evaluation system recalculates the composition of all particles. Consequently the iron content is set to zero and the appropriate contents of all other alloying elements, with contents greater 1 *wt.*-%,

are subtracted. The elemental composition of each particle is then renormalised to a total of 100 %. The mathematical details are given in **Eqs. (7-1)**–**(7-4)**:

$$x_{i_{FeCorr}} = \frac{x_i}{1 - \frac{x_{Fe}}{100}} \tag{7-1}$$

$$x_{i_{ECorr}} = x_{i_{FeCorr}} - \frac{x_{Fe} \cdot c_i}{c_{Fe}} \tag{7-2}$$

$$x_{i_{stand}} = \frac{x_{i_{ECorr}}}{1 - \frac{\sum_i x_{i_{ECorr}}}{100}} \tag{7-3}$$

Substituting **Eq. (7-2)** in **Eq. (7-3)** finally yields:

$$x_{i_{stand}} = \frac{x_{i_{FeCorr}} - \frac{x_{Fe} \cdot c_i}{c_{Fe}}}{1 - \frac{\sum_i \left(x_{i_{FeCorr}} - \frac{x_{Fe} \cdot c_i}{c_{Fe}} \right)}{100}} \tag{7-4}$$

In **Eqs. (7-1)**–**(7-4)** the symbols signify:

x_i ..... *wt.*-% of the element i in the particle

x_{Fe} ..... *wt.*-% of iron in the particle

c_i ..... *wt.*-% of the element i in the matrix

c_{Fe} ..... *wt.*-% of iron in the matrix

For the analysed steel PH 13-8 Mo the alloying elements given in **Tab. 7-1** are corrected:

Table 7-1: *Elements corrected for analysis of PH 13-8 Mo.*

Element	*wt.*-%
Cr	12.70
Ni	8.10
Mo	2.20
Al	1.10

While Al is corrected by the offline evaluation system of the INCA, the same is not performed for the results of the P-SEM. Although the steel contains only approximately 1 *wt.*-% Al (according to chemical analysis), it is the most important inclusion forming

element in the present case and should consequently be corrected in order to obtain representative results.

7.1.3 Inclusion Cluster

An essential part of the present thesis is the adaptation of inclusion classes to the analysed steel grade PH 13-8 Mo. The inclusion cluster shown in **Tab. 7-2** is developed on the basis of the chemical composition of the PH 13-8 Mo as well as Slag ASTM Steel Analysis and numerous SEM/EDX investigations on the PH 13-8 Mo. The finding of these inclusion classes was achieved in an iterative process, continuously optimising the inclusion characterisation potential of the offline evaluation system through special defined limit values for each class.

These values are set by considering the already corrected *wt.*-% of the detected particles and continuously optimised by analysing the EDX spectra of still unidentified particles and a thereof resulting correction and adaptation of the limits. As a consequence the percentage of unidentified particles concerning PH 13-8 Mo can be reduced to a minimum with the finally defined settings.

Tab. 7-2 illustrates the classes finally adapted to the inclusion landscape of the PH 13-8 Mo including a short description as well as the limiting values.

Generally the evaluation system divides all detected particles into 25 different classes. All inclusions that contain a rather large matrix portion even after matrix correction, are either too small or are the result of so-called pixel errors and therefore excluded. The composition of particles that are categorised within the class Unid (unidentified) do not fit in any of the other 23 inclusion classes, since either the defined limit of a certain class is not reached or the inclusion type is unknown.

Due to the fact that the INCA-Auto-identification of nitrogen causes a problem for small particles, there are two different types of aluminium nitride inclusion classes. While all particles with detected contents of nitrogen – and an additionally matching Al content – are categorised into AlN, inclusions that do not contain nitrogen and are characterised by a significantly high Cr and Al content are summarised in the class AlN_2. These circumstances

Table 7-2: *Explanation of INCA inclusion classes.*

Class	Type	Description	Limit values in *wt.*-%
1	AlN	Aluminium nitride	Al> 20, N> 10
2	Al_2O_3	Aluminium oxide	Al> 10, O> 10, Mg< 5
3	AlN_2	Aluminium nitride (without detected nitrogen)	Al> 20, N< 5, Cr> 15
4	Cr-Carbide	Chromium carbide	Cr> 10, C> 10
5	Carbide	Carbides excepting Cr and Si carbides	C> 30, Cr< 10, Si< 15
6	Cr-Oxide	Chromium oxide	Cr> 15, O> 10
7	MA-Spinel	Magnesium-aluminium spinel	Al> 30, Mg> 5, O> 10
8	MnS	Manganese sulfide	Mn> 5, S> 5
9	VC	Vanadium carbide	V> 5
10	CO	Carbo-oxide	C> 50, O> 10
11	Al-Silicate	Aluminium silicate	Al> 30, Si> 8
12	SiO_2	Silicon oxide	Si> 10, O> 10
13	CaO	Calcium oxide	Ca> 10, O> 10
14	CaS	Calcium sulfide	Ca> 20, S> 5
15	CaO-CaS	Calcium oxide with calcium sulfide	Ca> 10, O> 10, S> 10
16	MgO	Magnesium oxide	Mg> 10, O> 10
17	Mo-Oxide	Molybdenum oxide	Mo> 10, O> 10
18	MgS	Magnesium sulfide	Mg> 10, S> 10
19	SiC	Silicon carbide	Si> 10, C> 20
20	OS	endogenous oxide with sulfide	O> 15, S> 10
21	OCN	Oxi-carbo nitride	O> 15, N> 15, C> 15
22	CN	Carbo-nitride	C> 15, N> 15
23	CN-S	Carbo-nitride with sulfide	C> 15, N> 15, S> 10
24	Unid	Particle not categorised	no limit values
25	Excluded	high matrix portions-no identification possible	Fe> 80, Cr> 80, Si> 90, Mo> 20

are illustrated in **Fig. 7-6** and **Fig. 7-7**, where the same particle is analysed – once with an automated analysis and once conventionally with a larger magnification.

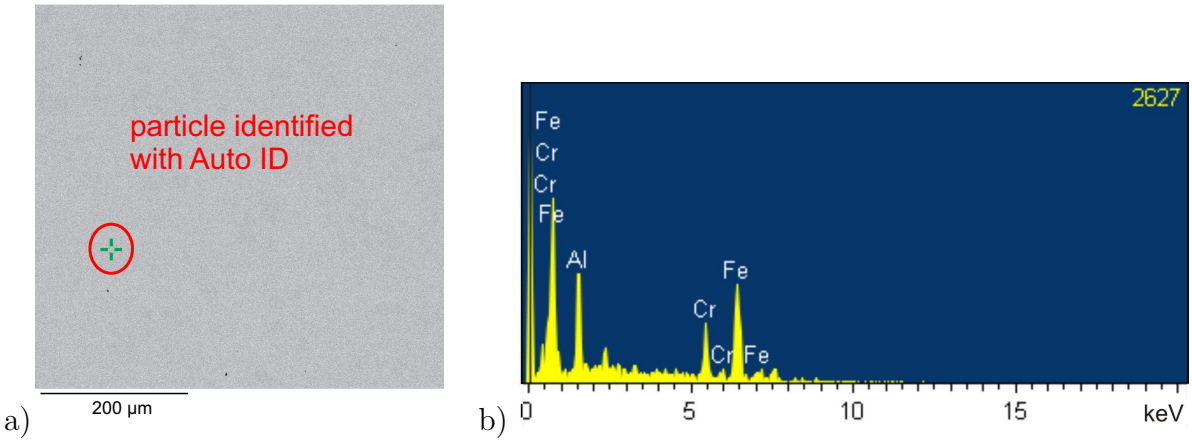

Figure 7-6: *a) Particle identified with Auto ID and b) Corresponding EDX spectrum.*

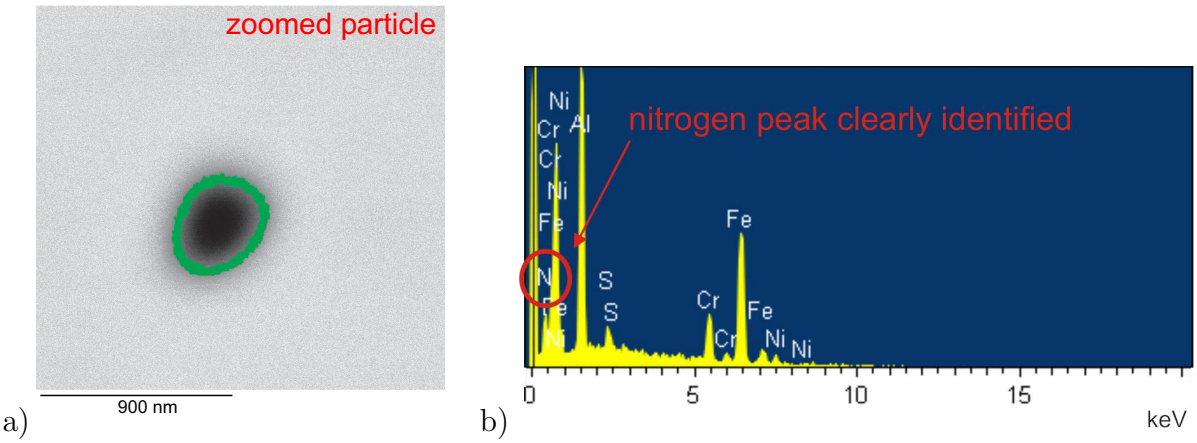

Figure 7-7: *a) Particle specially zoomed and b) Corresponding EDX spectrum.*

Regarding the morphological data of this particle, which has an area of 0.73 μm^2, it becomes obvious that the size of the particle is the limiting factor concerning Auto-ID of the nitrogen peak. This differentiation is only made possible by detailed non-automated SEM/EDX investigations under the awareness of restrictions of the automated analysis.

7.1.4 Results for Samples A-D

With the aid of the adapted offline evaluation system, samples of the PH 13-8 Mo can be analysed in detail concerning inclusion types as well as size and area distribution. Moreover an overview of the whole analysed sample area gives information about any inclusion concentration at any point, thereby allowing to draw conclusions concerning sample homogeneity. In the following all these aspects are exemplified for sample A, in order to get an impression of the large amount of possibilities that are offered by this evaluation system.

A general information about most frequent inclusions and maximum size in sample A is given in **Fig. 7-8**. It is demonstrated that the predominant percentage of inclusions is characterised by an Equivalent Circle Diameter (ECD) of about 1 μm, the maximum detected inclusion size in this sample is 5 μm.

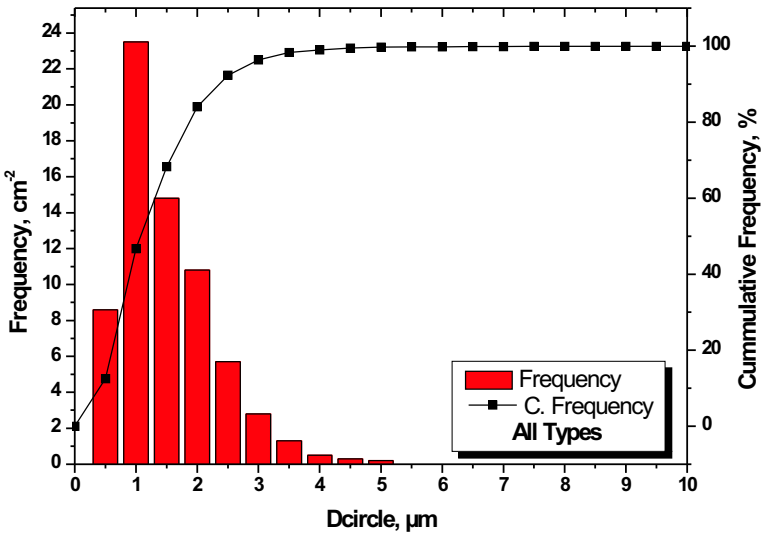

Figure 7-8: *Size distribution of all detected particles in sample A.*

Fig. 7-9 shows the inclusion types found in sample A and their corresponding area percentage regarding the analysed area of 100 mm^2.

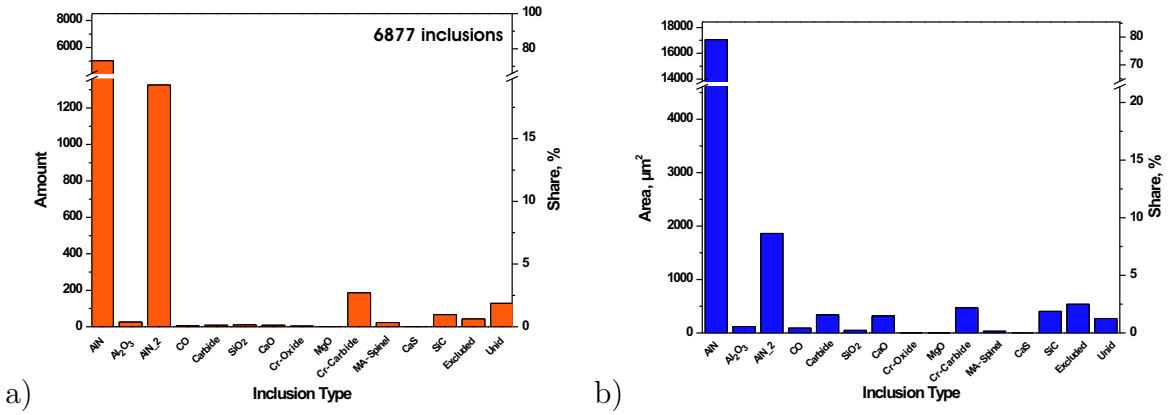

a) b)

Figure 7-9: *a) Inclusion types found in sample A and b) respective area distribution in sample A.*

The by far most frequent inclusion type are AlN, as already suggested by the conventional SEM/EDX investigations. This class also constitutes the largest area percentage, while it is noticeable that the area occupied by AlN_2 is comparatively small regarding the identified amount, underlining the fact that these inclusions are relatively small. Regarding the size distribution of the classes AlN and AlN_2 shown in **Fig. 7-10**, it can be observed that no detected AlN_2 is larger than 3 μm ECD, AlN however are characterised by a remarkable higher average ECD.

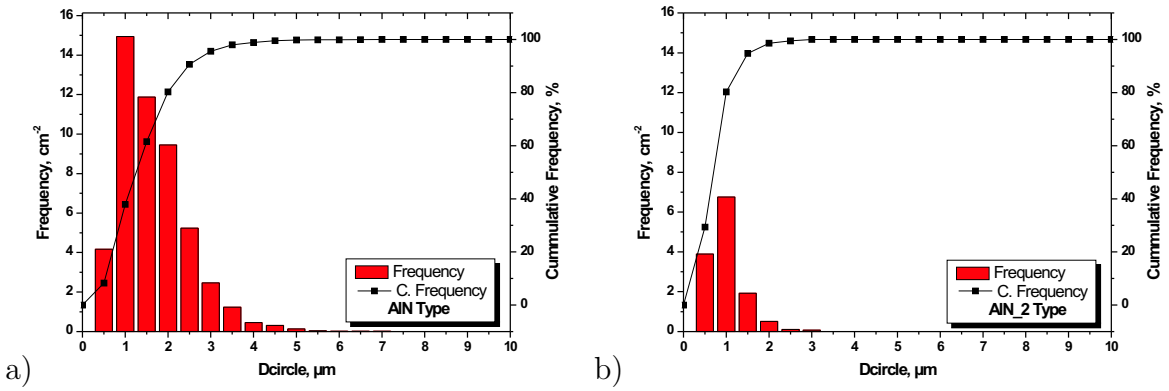

a) b)

Figure 7-10: *a) Size distribution of AlN in sample A and b) size distribution for AlN_2 in sample A.*

Sample B shows results similar to those of sample A – a high correlation is observed not only as far as detected inclusion amount is concerned, but also regarding the inclusion types. This dependency is shown in **Fig. 7-11** for the three most common inclusion types found in sample A and B. Seeing the fact that both samples were taken from the same

block only distinguishing themselves in the sampling orientation, it seems that the inclusions are isotropically distributed. In contrast to this a comparatively large difference can be discovered for samples C and D, which originate from prior process steps (admittedly not from the same melt as sample A and B).

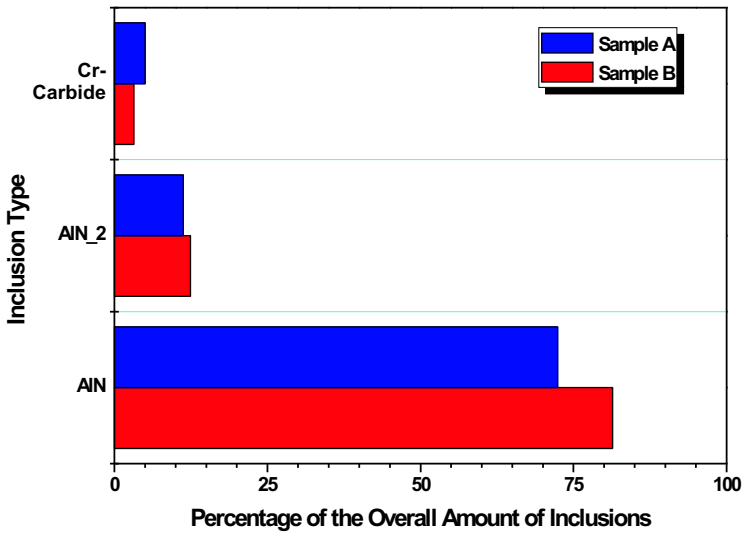

Figure 7-11: *Comparison of most frequently detected inclusion types in samples A and B.*

The overall amount of detected inclusions in sample C is approximately twice that of sample A. As shown in **Fig. 7-12a** the contents of Cr-Carbide and Al_2O_3 are significantly higher in sample C. Moreover the density distribution of detected particles illustrated in **Fig. 7-12b** shows a large agglomeration of inclusions in the right, bottom corner of the analysed area.

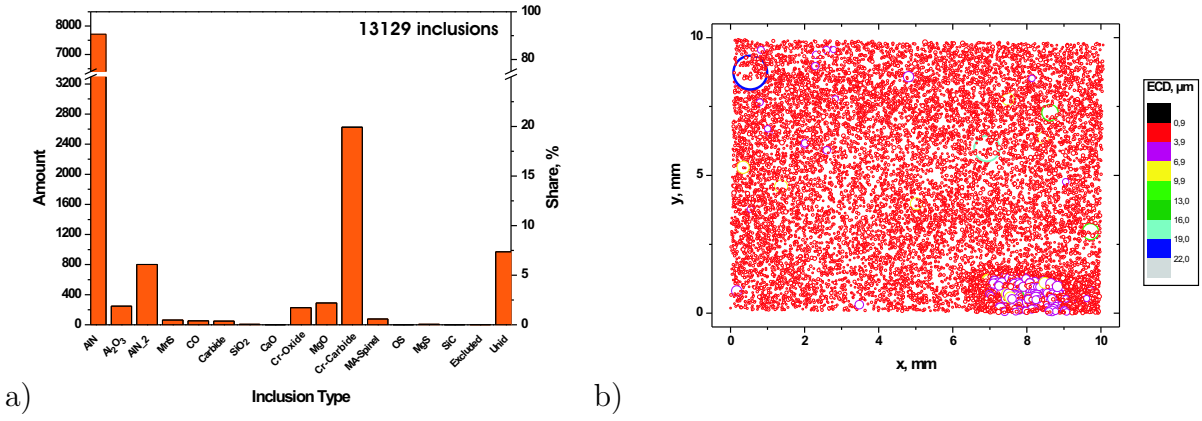

Figure 7-12: *a) Inclusion types found in sample C and b) Inclusion density for sample C.*

In sample D the lowest inclusion content of all four analysed samples is found. The detected inclusion types as well as the density distribution of particles in sample D is depicted in **Fig. 7-13**.

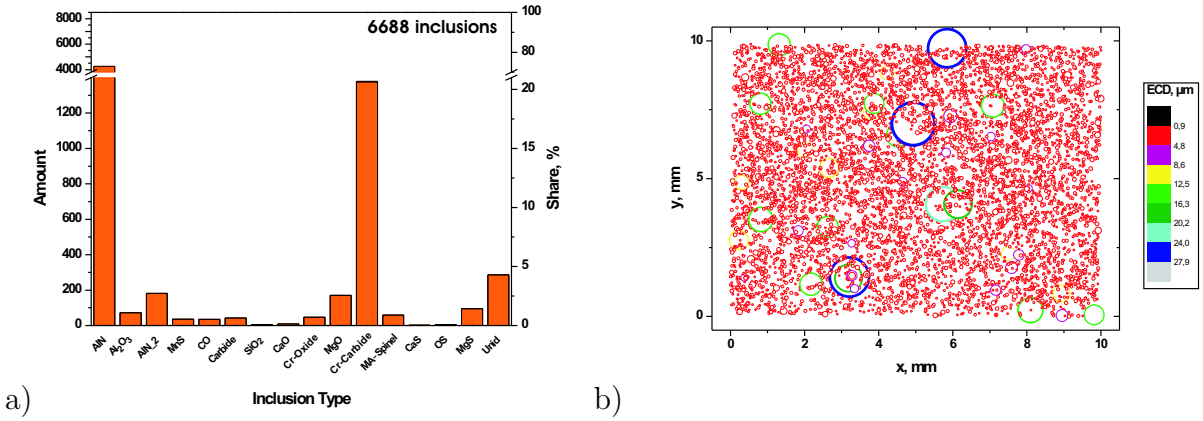

Figure 7-13: *a) Inclusion types found in sample D and b) Inclusion density for sample D.*

Comparing the size distributions of inclusions between sample C and D, the maximum is found in both cases at 1 μm ECD as demonstrated in **Fig. 7-14**.

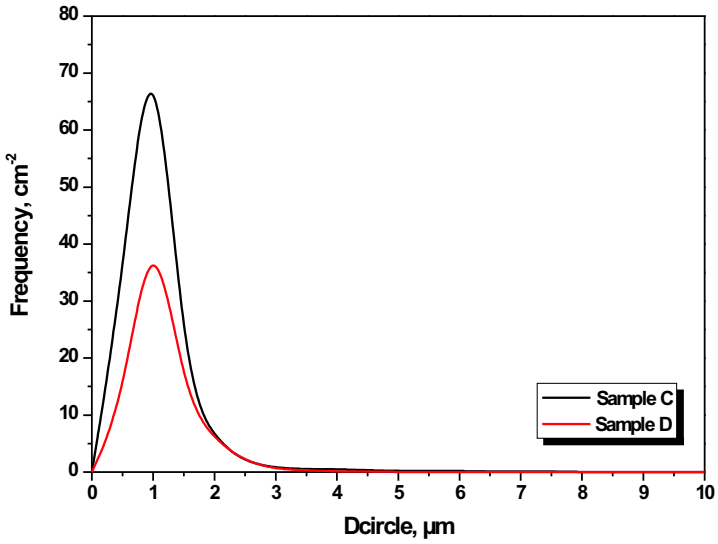

Figure 7-14: *Comparison of size distributions of sample C and D.*

7.2 Influencing Parameters

Based on this defined inclusion cluster, further automated SEM/EDX analyses are made in order to find optimal settings for inclusion characterisation. Several possible factors affecting the finally received results have been described in chapter 6. Subsequently, the influence of magnification and resolution is scrutinized. Moreover the sample homogeneity is tested in order to ascertain the validity of this method. Lastly, the applicability of the defined inclusion cluster to another steel grade is examined.

7.2.1 Magnification and Resolution

In order to examine the influence of magnification and resolution, a defined area of sample A is analysed with various combinations, shown in **Tab. 7-3**.

Table 7-3: *Analysed combinations of magnification and resolution – INCA.*

No.	Magnification	Resolution
1	300×	1024×960
2	600×	512×480
3	600×	1024×960
4	600×	2048×1920
5	1200×	1024×960

For reasons of comparability, the P-SEM settings are listed in **Tab. 7-4**, although the position of the analysed area differs between the P-SEM and the INCA trials.

Table 7-4: *Analysed combinations of magnification and resolution – P-SEM.*

No.	Magnification	Resolution
0	600×	2048×1920

While type and distribution of inclusions are little influenced, the parameter most affected by changing one of these properties is the amount of detected inclusions. As illustrated in

Fig. 7-15, a decreasing magnification and resolution results in a higher number of so-called pixel errors and consequently in a higher content of excluded particles.

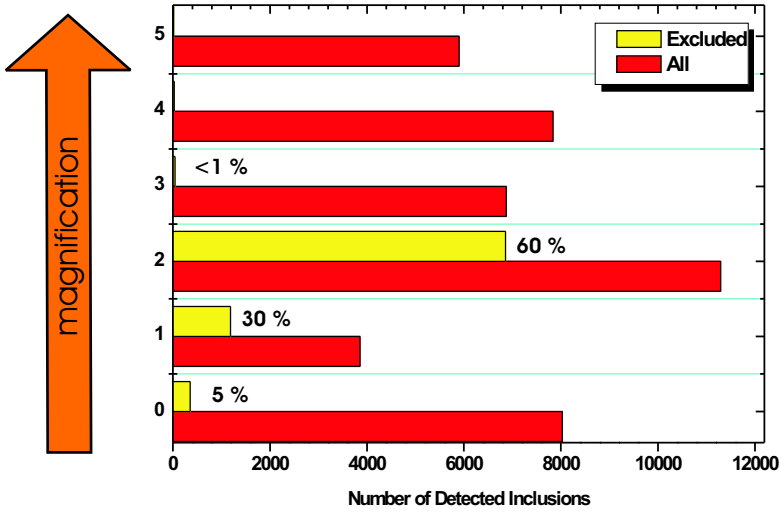

Figure 7-15: *Results of sample A with different combinations of magnification and resolution.*

Hence the number of pixels per unit seems to be decisive for the detection of a relatively representative amount of inclusions. A statistic concerning analysis time in dependence of the amount of detected inclusions is illustrated in **Fig. 7-16**. In this diagram the excluded fraction has already been subtracted from the overall amount. It is obvious that in the case of number 2 the analysis time is extremely high due to the large sum of detected particles, although not even 5000 of them can be categorised. Consequently this combination is definitely the least adequate for practical use. Even though the analysing time for combination number 1 is comparatively short, it is also not applicable regarding the fact that a magnification of 300× is not sufficient for inclusion sizes $< 1\ \mu m$. This context is shown in **Fig. 7-17**, where the difference in the detected amount of inclusions between a magnification of 300× and 600× for the same resolution settings is directly compared.

Although larger particles are detected in both cases, a significant difference concerning the frequency and density of smaller inclusions can be observed. Moreover the percentage of AlN_2 increases with decreasing magnification and resolution, whereby difficulties concerning the identification of nitrogen can be suggested using such a combination, also illustrated in **Fig. 7-18**.

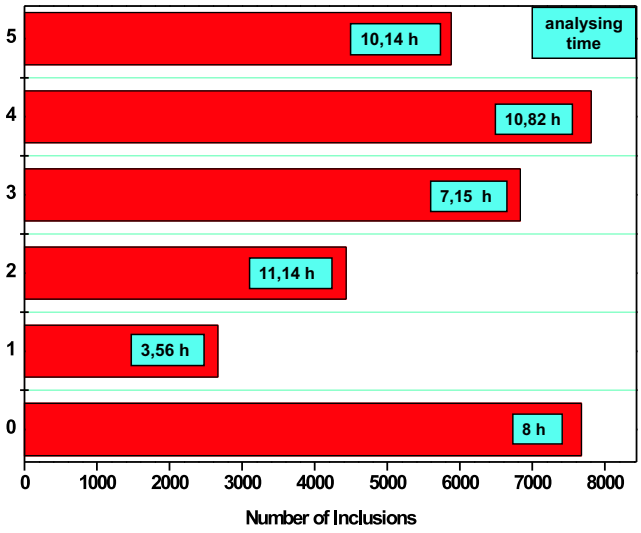

Figure 7-16: *Statistic of analysing time in dependence of the amount of detected inclusions.*

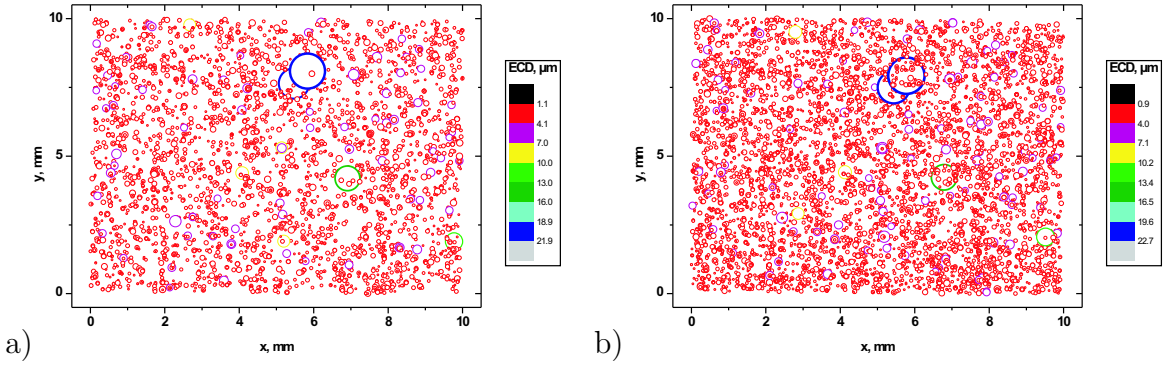

Figure 7-17: *a) Inclusion density at a magnification of 300 and b) inclusion density at a magnification of 600.*

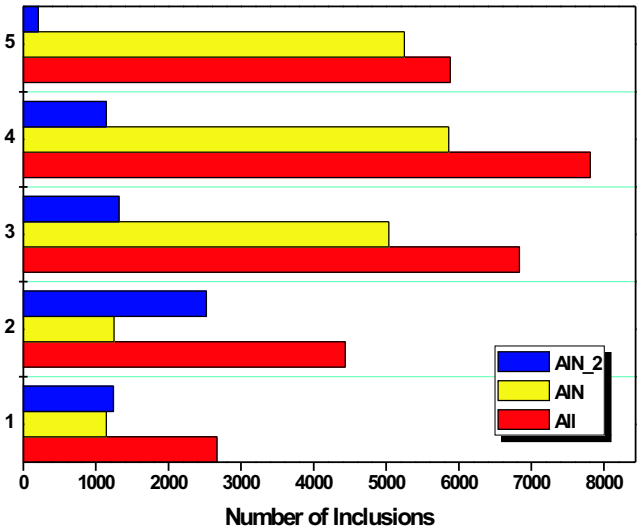

Figure 7-18: *Influence of magnification and resolution decrease on the identification of the nitrogen peak.*

When regarding combination number 4 together with the P-SEM results (number 0) it becomes apparent that the analysing time of the P-SEM is remarkably shorter using the same magnification and resolution settings. The reason for this time saving has already been described in chapter 5. In the case of number 3, where a smaller resolution is used, a comparable amount of inclusions is detected in considerably shorter time. It follows that a further increase of magnification or resolution will not lead to considerably better results that an increase of analysing time would be justified. Out of this reason the most applicable combination is number 3 – meaning a magnification of 600× and a resolution of 1024×960. This combination is hence used for all further investigations.

7.2.2 Sample Homogeneity

In order to prove the representativeness of the analysed sample area of 1 cm^2 and to get an impression of the sample homogeneity, a surface area of 4 cm^2 on sample G is divided into 4 equal analysing fields as illustrated in **Fig. 7-19**.

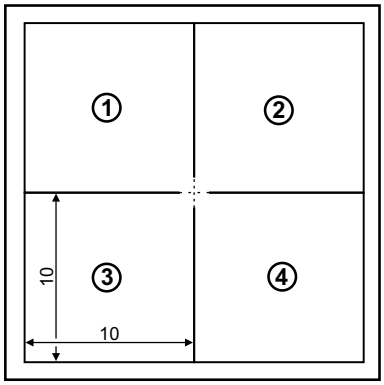

Figure 7-19: *Division of sample G.*

Each field was analysed with completely identic settings. **Fig. 7-20** shows the inclusion distribution over the analysed area for all four fields – the detected amount is approximately the same in all four cases, although it is remarkable that especially in field 2 several inclusions larger than 25 μm are observed. The maximum inclusion size in the other fields is about 20 μm, thereby confirming the assumption that large inclusions are less frequent and therefore more unlikely found than particles with an ECD smaller than 3 μm.

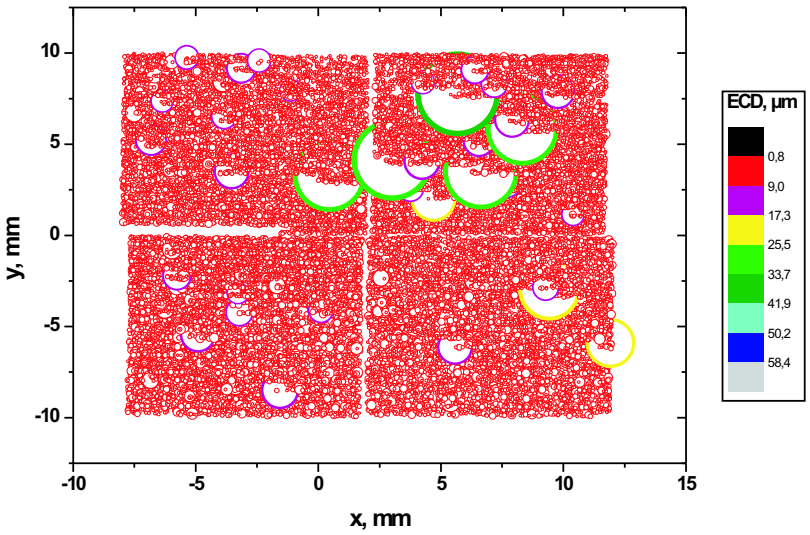

Figure 7-20: *Inclusion distribution for all 4 fields of sample G.*

Regarding the inclusion types found on the four fields demonstrated in **Fig. 7-21**, an accordance can be noticed, not only in type classes but also in the detected amount. As expected, more than 80 % of the detected particles are AlN, followed by a remarkably high content of Cr-Carbide, MgO and MA-Spinels. **Fig. 7-22** shows however discrepancies concerning the size distribution, although the larger inclusions of field 2 are not considered.

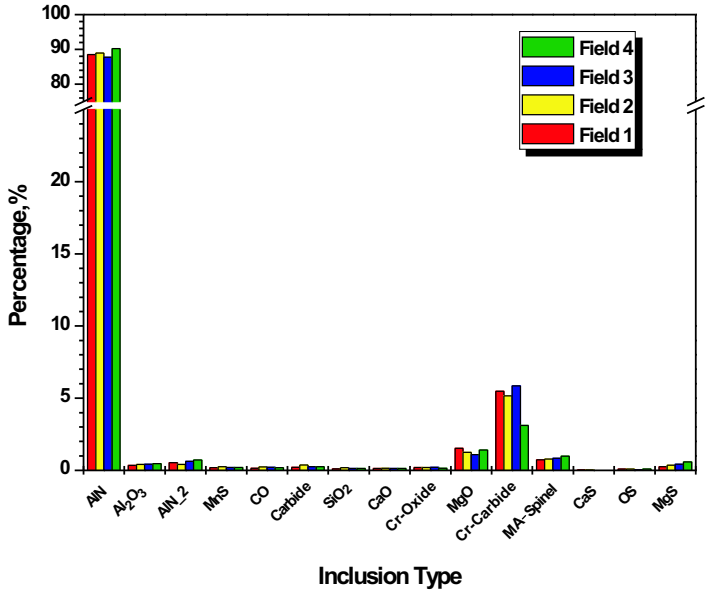

Figure 7-21: *Comparison of inclusion types found on sample G.*

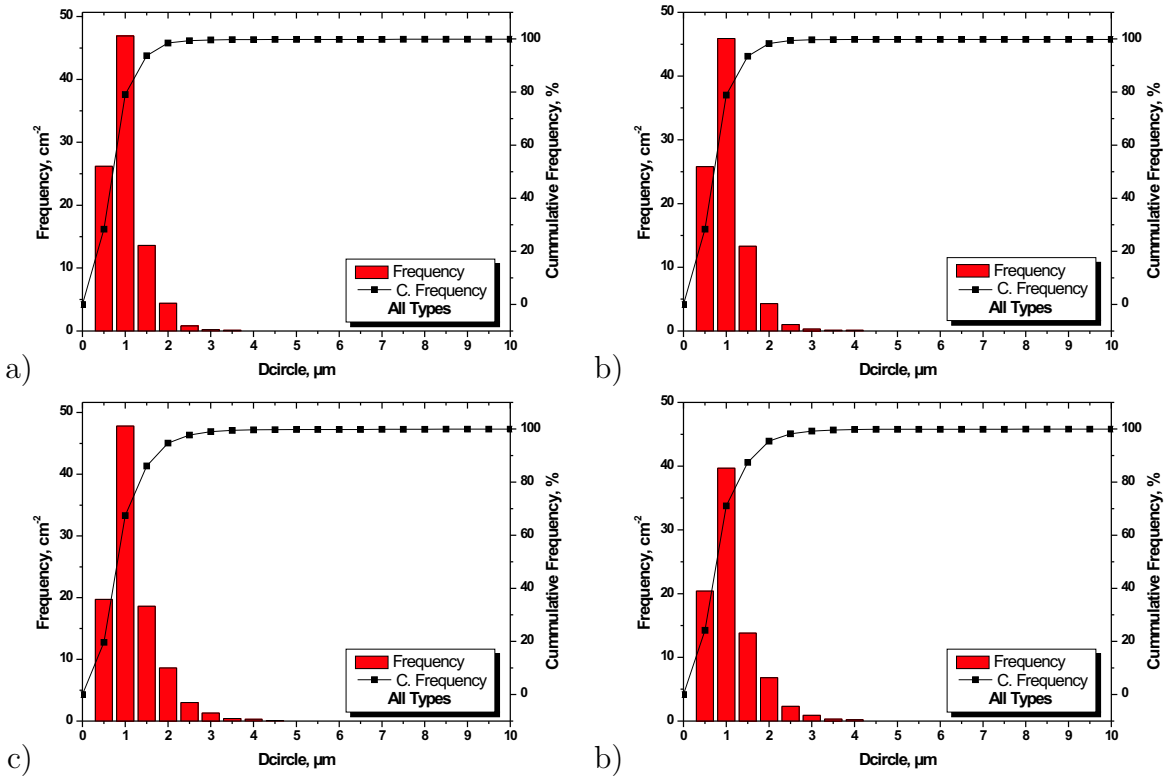

Figure 7-22: *a) Size distribution in field 1, b) size distribution in field 2, c) size distribution in field 3 and d) size distribution in field 4.*

7.2.3 Applicability to other Steel Grades

As already mentioned the described inclusion cluster is specially adapted to steel grade PH 13-8 Mo. In order to prove the applicability of this cluster to other steel grades produced at Böhler Edelstahl GmbH, the hot working steel H11, named sample I in the present thesis, is analysed with the offline evaluation system. The average chemical composition is given in **Tab. 7-5**.

Table 7-5: *Chemical composition of sample I in wt.-% [8].*

% C	% Si	% Mn	% Cr	% Mo	% V
0.38	1.10	0.40	5.00	1.30	0.40

Due to the fact, that this is a completely different steel grade, the matrix correction has to be changed, in order to assure a correct inclusion analysis. Following the same way as described in section 7.1.2 the three elements Si, Cr and Mo are corrected for analysing

sample I. Nonetheless the inclusion classes as well as the limiting values are not modified. **Fig. 7-23** shows the inclusions types found in sample I, which are naturally different to the inclusion landscape of the PH 13-8 Mo. In contrast to the PH 13-8 Mo, where AlN is the predominant inclusion type, the H11 is characterised by a comparatively low content of Alumina inclusions. Moreover, the percentage of Cr-Carbides is significantly lower in the case of H11 than for the PH 13-8 Mo, against what a comparable amount of MA-Spinels can be observed.

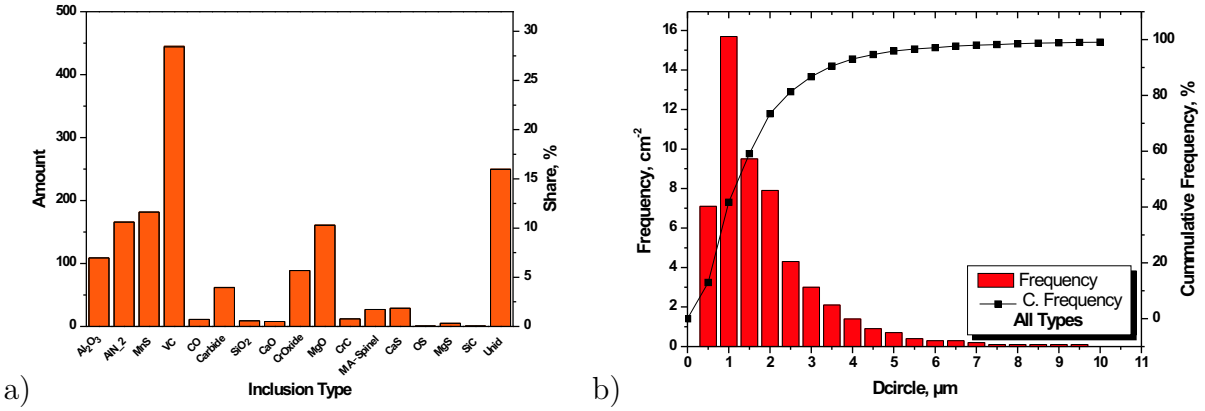

Figure 7-23: *a) Inclusion types found in Sample I and b) size distribution of inclusions in sample I.*

Although the most frequently detected inclusion type is VC, followed by MnS, MgO and AlN_2, the particulary noticeable fact is the high percentage of not identified particles, which is significantly higher than for the PH 13-8 Mo samples (resulting from the fact that the inclusion classes were adapted for the PH 13-8 Mo). As far as size distribution of inclusions in sample I is concerned, it is interesting to note that the inclusion size varies in a significantly wider range than for the PH 13-8 Mo, although the overall amount of detected inclusions is lower than for the PH 13-8 Mo. Additionally considerably more inclusions $> 5\ \mu m$ ECD are detected. Nevertheless more than 80 % of all particles are categorised within the inclusion cluster what seems remarkable and therefore shows a satisfactory degree of applicability.

7.3 Comparison of INCA and P-SEM Results

Several samples are analysed with INCA as well as P-SEM in order to obtain a comparison between both methods. As already described in chapter 5, the offline evaluation system of

P-SEM uses completely different inclusion classes. In the following a comparison between INCA and P-SEM results is shown for samples A, C and D. **Fig. 7-24a** shows the result of sample A analysed with the P-SEM offline evaluation system. Inclusion type A, meaning Al_2O_3 is the by far most often categorised type, as a consequence of the detected aluminium content. All particles that contain a sufficient amount of Al are ranked among this group lacking a differentiation between aluminium oxides and nitrides. The overall detected amount of inclusions can be compared to INCA results, keeping in mind that not the exactly same position on the sample is analysed.

The distribution of inclusion types for samples B, C and D is similar to that of sample A. Regarding the area distribution of inclusions on sample A in **Fig. 7-24b**, it can be seen that nearly 90 % of the area covered by inclusions is occupied by the inclusion type A.

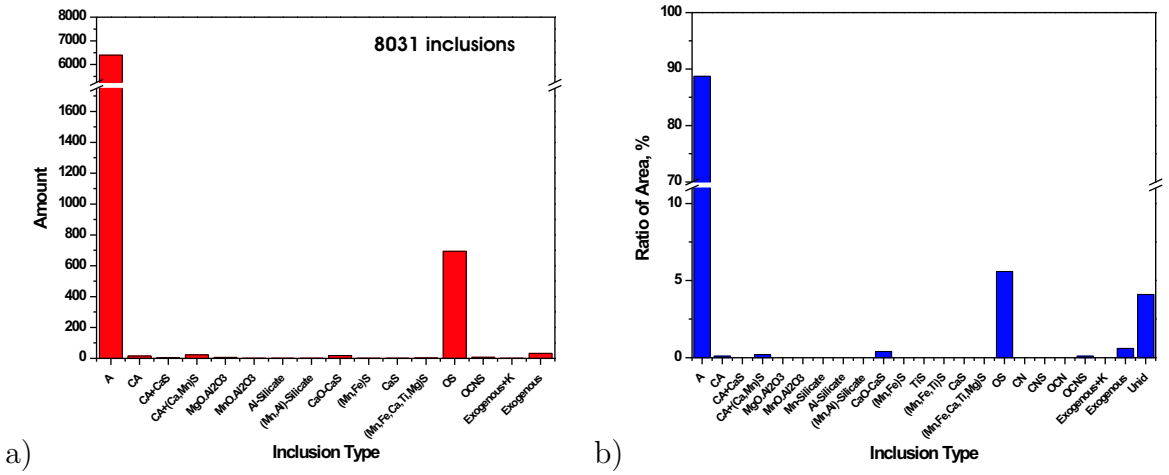

Figure 7-24: *a) P-SEM inclusion types found on sample A and b) Area distribution of inclusions on sample A.*

A difference between P-SEM and INCA results is also observed concerning detected inclusion sizes as illustrated in **Fig. 7-25**, where size distributions of P-SEM and INCA are compared. It is obvious that INCA detects more particles at sizes $< 1.5\ \mu m$, while the situation is changed as far as sizes $> 1.5\ \mu m$ are concerned.

On the whole, the overall amount of detected inclusion is approximately the same. Due to the lacking knowledge of exact P-SEM detection settings, it is difficult to give a reason for this context. A possible explanation could be different detection settings on the one hand, or the influence of the higher resolution on the other.

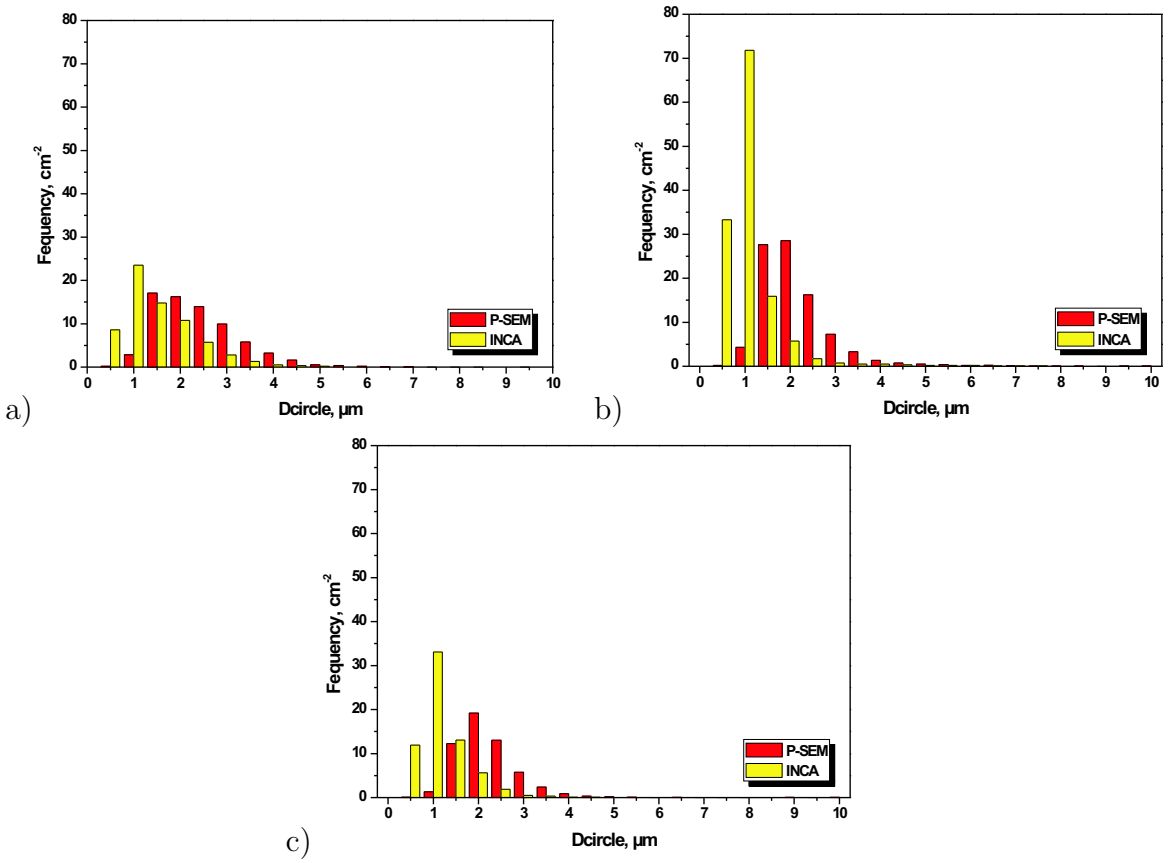

Figure 7-25: *a) Size distributions in sample A, b) size distributions in sample C and c) size distributions in sample D.*

7.4 Results for Samples E-H

In order to observe the inclusion development and modification over the process flow, samples E-H are taken out of the same melt at different process steps. Regarding **Fig. 7-26**, where the inclusion types found in sample H, meaning the remelted and rolled material, are shown, the same trend as already observed for sample A can be noticed: AlN is the most frequent detected inclusion class. **Fig. 7-27** shows the area distribution of sample H.

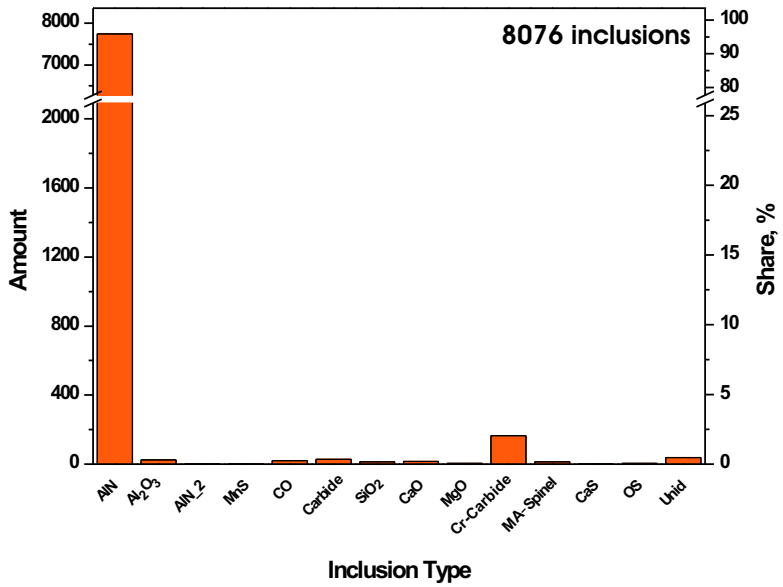

Figure 7-26: *Inclusion types found on sample H.*

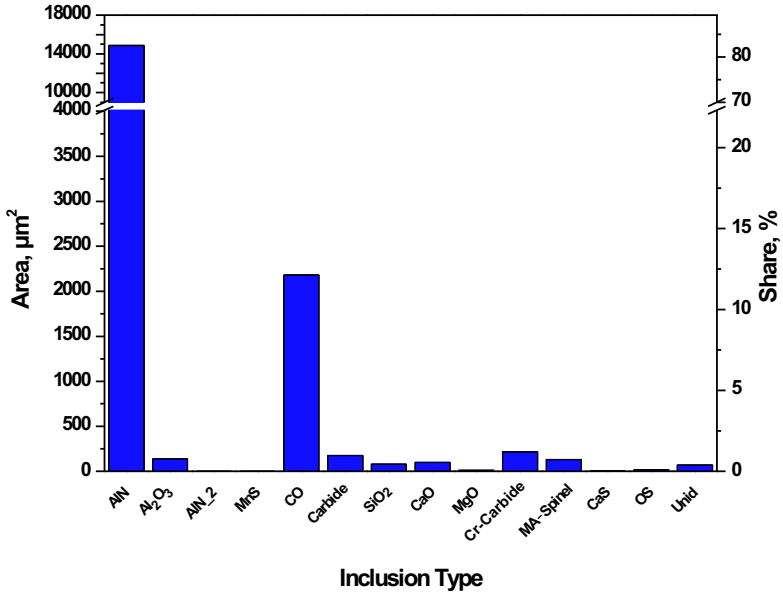

Figure 7-27: *Area distribution of inclusions on sample H.*

As illustrated in **Fig. 7-28** aluminium nitrides also dominate the inclusion landscape in samples E, F and G, which are taken from prior process steps. Concerning the overall detected inclusion amount, a similar tendency to that of samples A-D is observed. The results of samples A and C have already hinted at the fact that samples taken directly from the VIDP (sample E in the present case) are characterised by a double amount of particles compared to sample H, while sample G is situated near samples H concerning the overall detected particles.

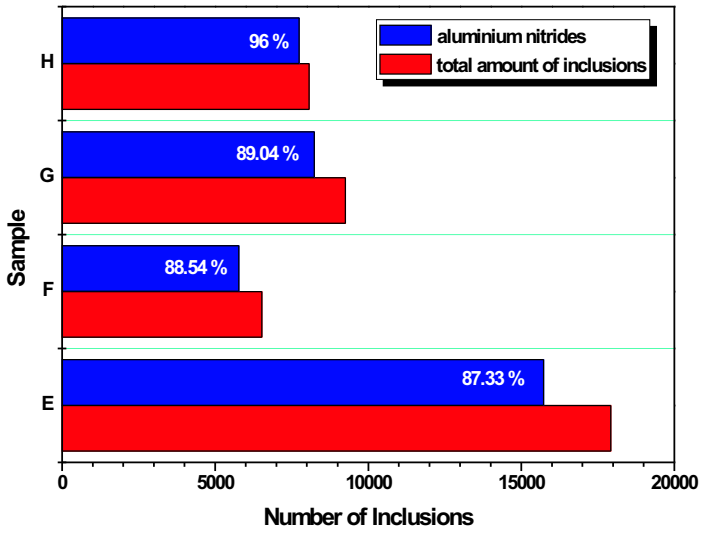

Figure 7-28: *Comparison of the overall detected inclusion amount in samples E-H.*

Interesting details however appear regarding the percentages of other inclusion classes found in these four samples. **Fig. 7-29** shows the most frequently detected inclusion types apart from aluminium nitrides. Especially sample G features a comparatively high Cr-Carbide content – against that less than 0.05 % Cr-Carbide are found in sample F. As demonstrated in **Fig. 7-30**, the Al_2O_3 content in sample H, meaning the rolled material, is significantly lower than in samples E and F, against what no clear trend can be observed for the MA-Spinel.

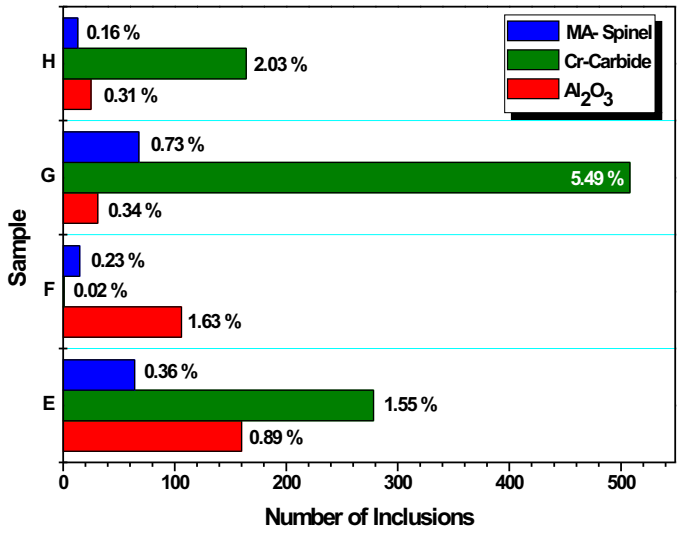

Figure 7-29: *Inclusion types next to aluminium nitrides found in samples E–H.*

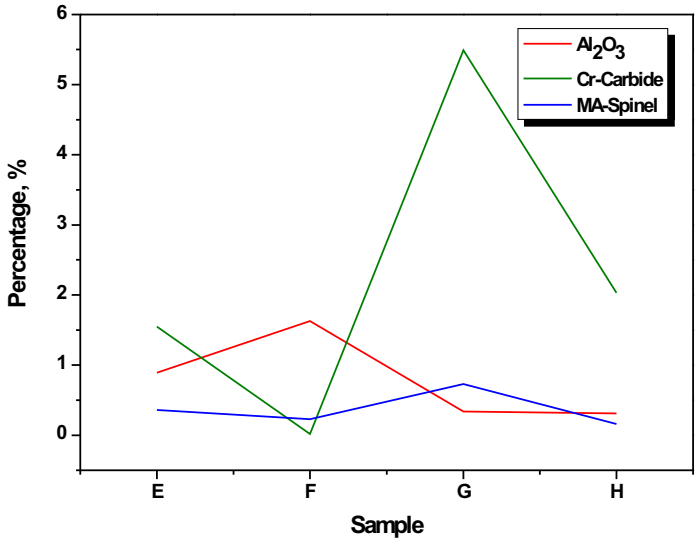

Figure 7-30: *Characteristics of Al_2O_3, MA-Spinel and Cr-Carbide over the process flow.*

Regarding the size distribution over the process flow for samples E-H as shown in **Fig. 7-31**, a clear maximum can be noticed at an inclusion size of 1 μm for all four samples, keeping in mind that the overall inclusion amount of particles is significantly higher in the case of sample E.

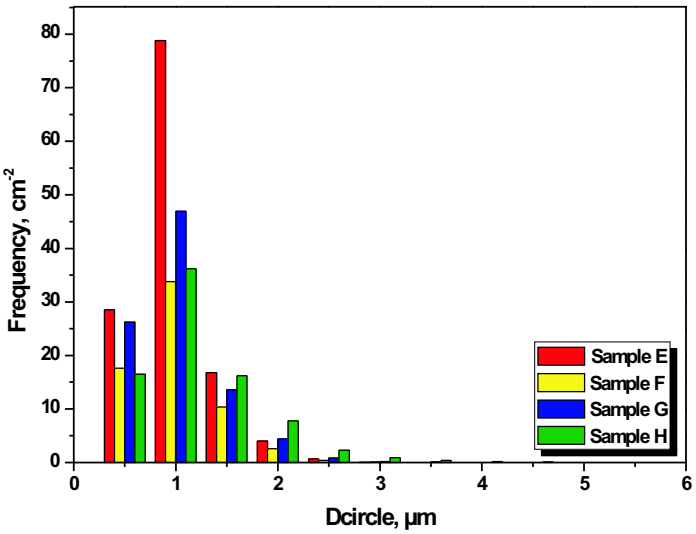

Figure 7-31: *Size distributions of samples E–H.*

In order to compare the density distribution of the four samples, an overview on each analysed sample area is shown in **Fig. 7-32**. A large decrease of the inclusion density between sample E, taken out of the VIDP and the final rolled material of sample H is

obvious. Moreover, apart from one inclusion with an ECD between $30-40\ \mu m$, a relatively homogenous distribution of the particles can be noticed in sample H. In contrast to this sample G and especially sample E feature a denser and partly less homogenous distribution, whilst a similar image to sample H arises for sample F.

The analysis of the described samples taken of the same melt, allows an insight on changes concerning the inclusion landscape over the process flow. Sample H for example is characterised by a significantly smaller amount of detected inclusions and a more homogenous distribution as compared to sample E, which is neither remelted nor rolled. As far as the most frequent inclusion type and size distribution between $1-5\ \mu m$ is concerned, no essential changes are observed over the process flow. Regarding the appearance of larger particles a higher percentage is found in not remelted and rolled material.

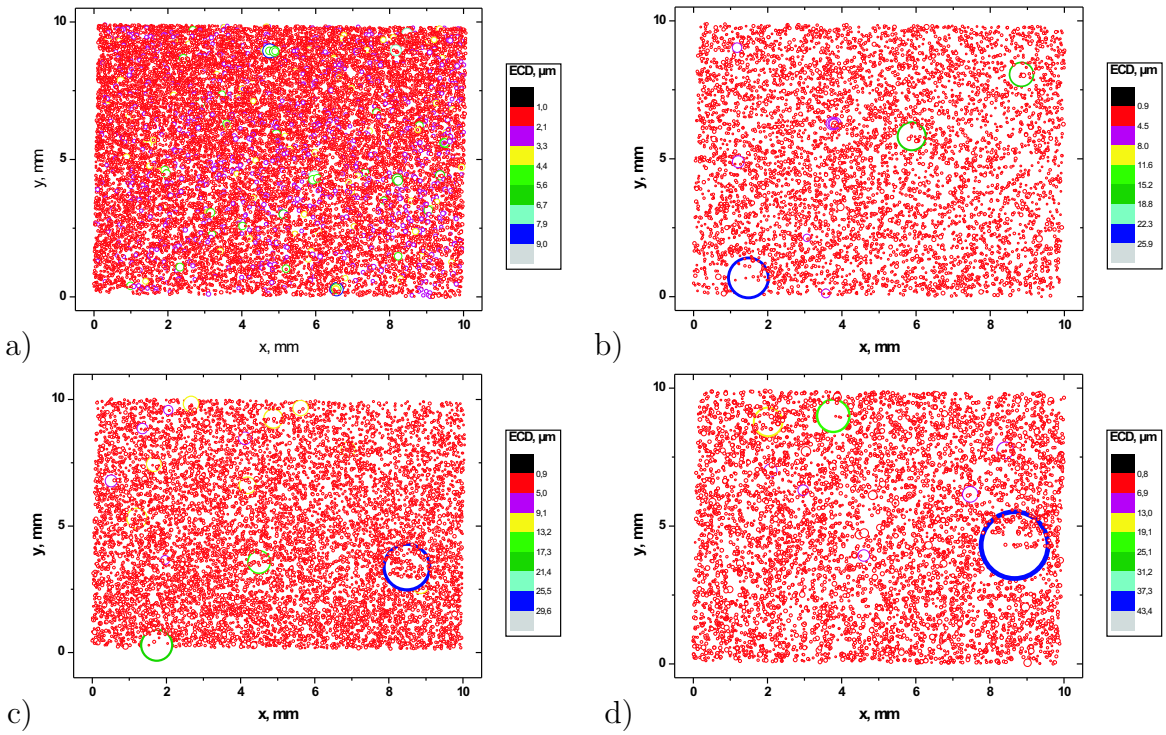

Figure 7-32: *a) Density distribution in sample E, b) density distribution in sample F, c) density distribution in sample G and d) density distribution in sample H.*

8 Summary and Conclusion

In the present thesis the basic interest was a further development of the inclusion characterisation for steel grades especially applied in the aerospace industry. The analysed steel grade is the precipitation hardenable martensitic steel PH 13-8 Mo, which combines the properties of stainless and maraging steels, and is therefore characterised by a considerable corrosion resistance as well as a remarkable hardness and tensile strength. Based on this alloying concept and the thereof resulting position inside the group of stainless steels, its mechanical and physical properties have been discussed. Moreover the theoretical background behind precipitation hardening of the PH 13-8 Mo, which is primarily achieved by the precipitation of the intermetallic compound NiAl, has been described. In order to ensure the micro cleanliness which is critical for the high fracture toughness of safety components, vacuum metallurgy is necessary. It has been shown that a double melting process (VIM/VAR) is essential for the fabrication of PH 13-8 Mo.

Nevertheless the formation of nonmetallic inclusions cannot be avoided during fabrication. Out of this reason the general possibilities for inclusion formation and classification as well as their influence on steel microstructure and resulting properties have been discussed. In order to prevent material failure by applying unclean steels, several methods of characterising inclusions for the evaluation of microscopic as well as macroscopic cleanliness were developed over the years. In the present work some of the most common methods for an analysis of the microscopic inclusion landscape have been discussed, pointing at the general statistical problem that arises when dealing with inclusion analysis as far as representativeness and reproducibility are concerned. Under this aspect advantages and disadvantages of Common Chart Comparison, OES-PDA, Computer Tomography, Electron Probe Micro Analysis and SEM/EDX investigations have been contrasted. Although the possibilities of application are very different and none of the methods meets the whole spectrum of expectations, each of them offers a special aspect that justifies its employment. Consequently no general ranking is possible and the best method has to be chosen depending on the particular application, in consideration of its advantages as well as limits of applicability.

A special focus of this thesis was set on automated methods for inclusion characterisation, which makes it possible to determine chemical composition, size, shape and position of a large amount of nonmetallic inclusions automatically. Compared to common methods, these methods offer significant advantages, like the larger range of size detection capability and the increased number of detectable inclusions. Furthermore obtaining enough individual inclusions to produce statistically significant information is very time consuming for a manual analysis. Lastly the recovery of a single inclusion in the presence of thousands can be difficult or even impossible.

In the practical part two different types of analysing equipments have been used for an automated inclusion analysis: Firstly the INCA system installed at the Chair of Metallurgy at the University of Leoben and secondly the Personal Scanning Electron Microscope (P-SEM) installed at voestalpine Stahl GmbH in Linz. Both methods are coupled with a special offline evaluation system including a matrix correction as well as an inclusion cluster to categorise the detected particles. In the case of P-SEM the defined inclusion classes are specially adapted to steel grades produced at voestalpine Stahl GmbH, where the most are different to those of Böhler Edelstahl GmbH. As a consequence a reasonably adapted inclusion cluster consisting of 25 inclusion classes had to be developed for the investigated steel grade. For a correct and representative classification a matrix correction was inevitable, because the number of generated X-rays at any point of a sample is influenced by a number of factors. Many iterations were required to find applicable limiting values for every inclusion class based on the already corrected $wt.$-% of the contained elements. Apart from AlN as the most frequently detected inclusion type, primarily Cr-Carbides, MA-Spinels and Aluminium Oxides were found when analysing samples taken from different process steps. The defined inclusion cluster was continuously optimised in the course of the present thesis.

Furthermore important parameters of the automated SEM/EDX analysis, like magnification and resolution, were tested on their influence on the amount and distribution of detected inclusions. Generally it was shown that a smaller magnification and a smaller resolution result in a more frequent emergence of so-called pixel errors – consequently also in a higher amount of excluded particles. Several combinations of resolution and magnification have been tested and an optimal adjustment was found using a magnification of 600× and a reso-

lution of 1024×960 in order to obtain representative results. A further increase of these two parameters did not make results so much more conclusive, as that the remarkable increase of analysing time were justified.

Moreover the representativeness of the analysing surface area of 1 cm^2 has been tested by investigating four different areas of this size on the same sample. Although the size distribution varies in a relatively wide range, approximately the same total amount of inclusions and their classification could be observed.

The evaluation system was also tested on its applicability to other steel grades. The analysed steel was the hot-work tool steel H11. Although a larger percentage of not identified particles was observed, more than 80 % of the overall amount of inclusions could be categorised in one of the defined classes. This shows a satisfying degree of applicability for the selected steel grades.

A comparison between P-SEM and INCA results for the same investigated samples gives information about the differences and problems of inclusion characterisation because of the large amount of influencing factors. In the case of P-SEM the inclusions are categorised without knowing their contents of nitrogen, carbon and oxygen (these elements are not detected in the EDX spectrum of the P-SEM). Consequently the offline evaluation system cannot differ between aluminium nitrides and oxides and classifies all particles, which contain a sufficient percentage of aluminium in the same class. Out of this reason the applicability of P-SEM inclusion classes to the PH 13-8 Mo is limited. Moreover a difference in size distribution has also been observed. While the overall amount of detected inclusions is comparable, the INCA system detects much more inclusions with a diameter $< 1.5\ \mu m$, while diameters $> 2\ \mu m$ are more frequently detected by the P-SEM. A possible reason could lie in the detection or grey scale value settings, since results are highly influenced by these settings.

A detailed inclusion investigation of four samples of the same melt – pursuing the inclusion development and modification over the process – completes the practical part of this thesis. It has been illustrated that the overall amount of inclusions is significantly lower after the remelting process. Additionally a more homogenous distribution of particles is reached by

remelting and rolling. Concerning the inclusion types, an accordance could be observed over the whole process flow, whereby aluminum nitrides are the most dominant inclusion type. Although the overall percentage of Al_2O_3 is relatively low, a decrease of Al_2O_3 could be determined in the rolled material compared to the sample taken out of the VIDP. As far as size distribution is concerned, a definite maximum was observed for inclusions with a diameter of app. 1 μm.

Finally it can be concluded that the application of the described inclusion cluster is a first step towards a further development of the inclusion characterisation for steel grades produced at Böhler Edelstahl GmbH. The applicability of the system could be enlarged by the definition of further inclusion classes resulting from exact and extensive SEM/EDX investigations. The employed automated method is definitely the best in order to obtain detailed and representative results concerning inclusion landscape, given an approximate knowledge about the possibly detected inclusion types.

Bibliography

[1] Jacobi, H.: Metallurgie und Werkstofftechnik hochreiner Stähle. Stahl und Eisen, Vol. 114 (1994), Nr. 11, 45–56.

[2] Stiller, K., F. Danoix and A. Bostel: Investigation of precipitation hardening in a new maraging stainless steel. Applied Surface Science, Vol. 94/95 (1996), No. 3, 326–333.

[3] Edelstahl-Vereinigung e.V. & Verein deutscher Eisenhüttenleute (Ed.): Nichtrostende Stähle. Verlag Stahleisen, Düsseldorf (1989).

[4] Verein deutscher Eisenhüttenleute (Ed.): Werkstoffkunde Stahl. Springer Verlag, Berlin (1985).

[5] Engl, B. (Ed.): Ausscheidungsatlas der Stähle. Verlag Stahleisen, Düsseldorf (1983).

[6] Brezina, P.: Martensitische CrNi-Stähle mit tiefem Kohlenstoffgehalt. Escher Wyss Mitteilungen 1/2 (1980), 218–236.

[7] Seetharaman, V., M. Sundararaman and R. Krishnan: Precipitation hardening in a PH 13-8 Mo stainless steel. Material Science and Engineering, Vol. 47 (1981), 1–11.

[8] Böhler Edelstahl GmbH (Ed.): Special Steel Manual. Private publishing, Kapfenberg (2006).

[9] Cieslak, M.J. et al.: An investigation of the high-temperature and solidification microstructures of PH 13-8 Mo stainless steel. Metallurgical Transactions A, Vol. 21A (1990), 2465–2475.

[10] Garrison, W.M. and J.A. Brooks: The thermal and mechanical stability of austenite in the low carbon martensitic steel PH 13-8. Material Science and Engineering A, Vol. 149 (1991), 65–72.

[11] Roth, M. and C. Lelièvre: Failure investigations of PH 13-8 Mo aircraft components. Microstructural Science, Vol. 26 (1998), 51–58.

[12] Patel, A.M., R.W. Neu and J.A. Pape: Growth of small fatigue cracks in PH 13-8 Mo stainless steel. Metallurgical and Materials Transactions A, Vol. 30A (1999), 1289–1300.

[13] Fahir Arisoy, C. et al.: Failure of a 17-4 PH stainless steel sailboat propeller shaft. Engineering Failure Analysis, Vol. 10 (2003), 711–717.

[14] Scheidl, H. and E. Krainer: Grundlagen und technologische Besonderheiten von Maraging-Stählen. Radex-Rundschau, (1977), 310–327.

[15] Gottstein, G.: Physikalische Grundlagen der Materialkunde. Springer Verlag, Berlin (2001).

[16] Ping, D.H. et al.: Microstructural evolution in 13Cr-8Ni-2.5Mo-2Al martensitic precipitation-hardened stainless steel. Material Science and Engineering A, Vol. 394 (2005), 285–295.

[17] Erlach, S.D. et al.: Comparison of NiAl precipitation in a medium carbon secondary hardening steel and C-free PH 13-8 maraging steel. Material Science and Engineering A, Vol. 429 (2006), 96–106.

[18] Guo, Z. and W. Sha: Thermodynamic calculations for precipitation hardening steels and titanium aluminides. Intermetallics, Vol. 10 (2002), 945–950.

[19] Robino, C.V. et al.: Heat treatment of investment cast PH 13-8 Mo stainless steel: part II – isothermal aging kinetics. Metallurgical and Materials Transactions A, Vol. 25A (1994), 697–704.

[20] De Almeida, L.H. et al.: A study of precipitation hardening in a PH 13-8 Mo stainless steel. Microstructural Sciene, Vol. 22, 441–447.

[21] Schumacher, W.J.: Armco PH 13-8 Mo the ultimate high strength stainless steel. 37th Annual Technical Meeting, Investment Casting Institute (1989).

[22] Heinen, K.H. (Ed.): Elektrostahl-Erzeugung. Verlag Stahleisen, Düsseldorf (1997).

[23] Krieger, W., C. Bernhard and J. Korp: Spezielle metallurgische Prozesstechnik, Lecture Script, University of Leoben (2006).

[24] Dahl, W.: Eigenschaften und Anwendung von Stählen. Augustinus Buchhandlung, Aachen (1993).

[25] Trenkler, H. and W. Krieger: Gmelin-Durrer Metallurgie des Eisens. Vol. 6, Springer Verlag, Berlin (1978).

[26] Angeli, J.: Prüftechnik und Analytik zur Einschlussbestimmung. Nichtmetallische Einschlüsse in Stählen, ASMET Seminar, Leoben (2006).

[27] Javojskij, V.I.: Theorie der Stahlerzeugung. Deutscher Verlag für Grundstoffindustrie, Leipzig (1969).

[28] Bleck, W. (Ed.): Werkstoffkunde Stahl für Studium und Praxis. Verlag Mainz, Aachen (2004).

[29] Atkinson, H.V. and G. Shi: Characterization of inclusions in clean steels: a review including the statistics of extremes methods. Progress in Material Science, Vol. 48 (2003), 457–520.

[30] Jacobi, H., H.-J. Bäthmann and J. Gronsfeld: Neuartige Bestimmung des Makro-Reinheitsgrades am unkonventionell gewalzten Strangguss. Stahl und Eisen, Vol. 108 (1988), Nr. 20, 946–958.

[31] Verein deutscher Eisenhüttenleute (Ed.): Stahleisenprüfblatt 1580, Stufendrehversuch zur makroskopischen Prüfung von Stählen auf nichtmetallische Einschlüsse. Verlag Stahleisen, Düsseldorf (1960).

[32] Jacobi, H. and K. Wünneberg: Improving oxide cleaness on basis of MIDAS method. Ironmaking and Steelmaking, Vol. 30 (2003), No. 2, 130–141.

[33] Deutsches Institut für Normung (Ed.): DIN 50602, Mikroskopische Prüfung von Edelstählen auf nichtmetallische Einschlüsse mit Bildreihen, Beuth Verlag GmbH, Berlin (1985).

[34] American Society for Testing and Materials (Ed.): Annual Book of ASTM Standards, Philadelphia (2002).

[35] Zhang, L. and B.G. Thomas: State of the art evaluation and control of steel cleanliness. ISIJ International, Vol. 43 (2003), No. 3, 271–291.

[36] Meilland, R. and L. Dosdat: Rapid characterization of inclusionnary cleanliness in steels by PDA-OES mapping. La Revue de Métallurgie-CIT, (2002), 373–382.

[37] Göransson, M. and P.G. Jönsson: Ideas for process control of inclusion characteristics during steelmaking. ISIJ International, Vol. 41 (2001), 42–46.

[38] Reinholdsson, F. et al.: A metallurgical tool for rapid determination of micro inclusion characteristics in bearing steel production. ISIJ International, Vol. 37 (1997), No. 6, 637–639.

[39] Pfeifer-Schäller, I. et al.: Computertomographie im Vergleich mit konventionellen Prüfverfahren. DGZfP-Jahrestagung, Berlin (2001).

[40] Sauerwein, C. et al.: Anwendungen der 3D-Computertomographie in Entwicklung und Forschung. DGZfP-Jahrestagung, Berlin (2001).

[41] Swoboda, K., R. Blöch and E. Plöckinger: Über die Castaingsche Mikrosonde und deren Einsatz im Edelstahlwerk. BHM, Vol. 108. (1963), 391–401.

[42] Wohlleben, K. et al.: Einsatz der Elektronenstrahl-Mikrosonde bei der Untersuchung nichtmetallischer Einschlüsse im Stahl. Radex-Rundschau, (1965), 524–536.

[43] Schmidt, P.F.: Praxis der Rasterelektronenmikroskopie und Mikrobereichsanalyse. Expert verlag, Renningen-Malmsheim (1994).

[44] Oxford Instruments: Wavelength dispersive X-ray microanalysis. Technical Briefing, Oxford Instruments Analytical Limited (2002).

[45] Flegler, S.L., J.W. Heckman and K.L. Klomparens: Elektronenmikroskopie. Spektrum Akad. Verlag, Heidelberg (1995).

[46] Oxford Instruments: Energy dispersive X-ray microanalysis hardware. Technical Briefing, Oxford Instruments Analytical Limited (2002).

[47] Nuspl, M. et al.: Qualtitative and quantitative determination of micro-inclusions by automated SEM/EDX analysis. Analytical and Bioanalytical Chemistry, 379 (2004), 640–645.

[48] Winkler, W., J.Angeli and M. Mayr.: Automated SEM/EDX cleanness analysis for metallurgical developments. Proceedings 7th International Workshop: Progress in analytical chemistry in the steel and metal industries, (2006), 281–288.

[49] Winkler, W., J.Angeli and M. Mayr.: Automated SEM-EDX cleanness analysis and its application in metallurgy. BHM, Vol. 152 (2007), 4–9.

[50] Böhler Edelstahl GmbH (Ed.): Böhler high-performance materials for the aircraft and aerospace industry. Private publishing, Kapfenberg (2006).